AFRL-AFOSR-VA-TR-2019-0314

# Toward Bio-Inspired Smart Thermal Spreaders (BSTS)

Hadi Ghasemi
UNIVERSITY OF HOUSTON SYSTEM

11/01/2019
Final Report

Air Force Research Laboratory
AF Office Of Scientific Research (AFOSR)/ RTB1
Arlington, Virginia 22203
Air Force Materiel Command

**REPORT DOCUMENTATION PAGE**

*Form Approved*
*OMB No. 0704-0188*

**1. REPORT DATE** *(DD-MM-YYYY)*
10/29/2019

**2. REPORT TYPE**
Final

**3. DATES COVERED** *(From - To)*
5/1/2016-7/30/2019

**4. TITLE AND SUBTITLE**
Toward Bio-Inspired Smart Thermal Spreaders (BSTS)

**5a. CONTRACT NUMBER**

**5b. GRANT NUMBER**
FA9550-16-1-0248

**5c. PROGRAM ELEMENT NUMBER**

**6. AUTHOR(S)**
Hadi Ghasemi

**5d. PROJECT NUMBER**

**5e. TASK NUMBER**

**5f. WORK UNIT NUMBER**

**7. PERFORMING ORGANIZATION NAME(S) AND ADDRESS(ES)**
University of Houston
4726 Calhoun Rd, Engineering Bldg I, Room N229, Houston, TX, 77389

**8. PERFORMING ORGANIZATION REPORT NUMBER**

**9. SPONSORING/MONITORING AGENCY NAME(S) AND ADDRESS(ES)**
Air Force Office of Scientific Research
875 Randolph Street
Suite 325 Room 3112
Arlington, VA 22203

**10. SPONSOR/MONITOR'S ACRONYM(S)**

**11. SPONSOR/MONITOR'S REPORT NUMBER(S)**

**12. DISTRIBUTION/AVAILABILITY STATEMENT**
Public

**13. SUPPLEMENTARY NOTES**
NA

**14. ABSTRACT**

In this research program, we aimed to understand fundamentals of liquid- vapor phase change at small-scale and to develop a bio-inspired thermal spreader. In the first budget period, we developed a new concept and corresponding material structure that breaks the limit of phase-change heat transfer (Leidenfrost limit). The developed concept, decoupled hierarchical structures, is implemented in both Si and Cu structures. In the second budget period, we studied fundamentals of liquid-vapor phase change in a controlled evaporation chamber to tune and measure interfacial mass and heat transfer at

**15. SUBJECT TERMS**
Thermal managemnet, Nanochannels,

**16. SECURITY CLASSIFICATION OF:**
**a. REPORT** U
**b. ABSTRACT** U
**c. THIS PAGE**

**17. LIMITATION OF ABSTRACT**
UU

**18. NUMBER OF PAGES**

**19a. NAME OF RESPONSIBLE PERSON**
Hadi Ghasemi

**19b. TELEPHONE NUMBER** *(Include area code)*
713-743-6183

## INSTRUCTIONS FOR COMPLETING SF 298

**1. REPORT DATE.** Full publication date, including day, month, if available. Must cite at least the year and be Year 2000 compliant, e.g. 30-06-1998; xx-06-1998; xx-xx-1998.

**2. REPORT TYPE.** State the type of report, such as final, technical, interim, memorandum, master's thesis, progress, quarterly, research, special, group study, etc.

**3. DATE COVERED.** Indicate the time during which the work was performed and the report was written, e.g., Jun 1997 - Jun 1998; 1-10 Jun 1996; May - Nov 1998; Nov 1998.

**4. TITLE.** Enter title and subtitle with volume number and part number, if applicable. On classified documents, enter the title classification in parentheses.

**5a. CONTRACT NUMBER.** Enter all contract numbers as they appear in the report, e.g. F33315-86-C-5169.

**5b. GRANT NUMBER.** Enter all grant numbers as they appear in the report. e.g. AFOSR-82-1234.

**5c. PROGRAM ELEMENT NUMBER.** Enter all program element numbers as they appear in the report, e.g. 61101A.

**5e. TASK NUMBER.** Enter all task numbers as they appear in the report, e.g. 05; RF0330201; T4112.

**5f. WORK UNIT NUMBER.** Enter all work unit numbers as they appear in the report, e.g. 001; AFAPL30480105.

**6. AUTHOR(S).** Enter name(s) of person(s) responsible for writing the report, performing the research, or credited with the content of the report. The form of entry is the last name, first name, middle initial, and additional qualifiers separated by commas, e.g. Smith, Richard, J, Jr.

**7. PERFORMING ORGANIZATION NAME(S) AND ADDRESS(ES).** Self-explanatory.

**8. PERFORMING ORGANIZATION REPORT NUMBER.** Enter all unique alphanumeric report numbers assigned by the performing organization, e.g. BRL-1234; AFWL-TR-85-4017-Vol-21-PT-2.

**9. SPONSORING/MONITORING AGENCY NAME(S) AND ADDRESS(ES).** Enter the name and address of the organization(s) financially responsible for and monitoring the work.

**10. SPONSOR/MONITOR'S ACRONYM(S).** Enter, if available, e.g. BRL, ARDEC, NADC.

**11. SPONSOR/MONITOR'S REPORT NUMBER(S).** Enter report number as assigned by the sponsoring/ monitoring agency, if available, e.g. BRL-TR-829; -215.

**12. DISTRIBUTION/AVAILABILITY STATEMENT.** Use agency-mandated availability statements to indicate the public availability or distribution limitations of the report. If additional limitations/ restrictions or special markings are indicated, follow agency authorization procedures, e.g. RD/FRD, PROPIN, ITAR, etc. Include copyright information.

**13. SUPPLEMENTARY NOTES.** Enter information not included elsewhere such as: prepared in cooperation with; translation of; report supersedes; old edition number, etc.

**14. ABSTRACT.** A brief (approximately 200 words) factual summary of the most significant information.

**15. SUBJECT TERMS.** Key words or phrases identifying major concepts in the report.

**16. SECURITY CLASSIFICATION.** Enter security classification in accordance with security classification regulations, e.g. U, C, S, etc. If this form contains classified information, stamp classification level on the top and bottom of this page.

**17. LIMITATION OF ABSTRACT.** This block must be completed to assign a distribution limitation to the abstract. Enter UU (Unclassified Unlimited) or SAR (Same as Report). An entry in this block is necessary if the abstract is to be limited.

# Final Report
# Air Force Office of Scientific Research

## FA9550-16-1-0248
## Program Manager: Dr. Ali Sayir

## Title of Research Project:
Toward Bio-Inspired Smart Thermal Spreaders (BSTS)

## Principle Investigator:
Hadi Ghasemi
Associate Professor
University of Houston

## Final Report
Performance period: 05/01/2016-07/30/2019

## Executive Summary

In this research program, we aimed to understand fundamentals of liquid-vapor phase change at small-scale and to develop a bio-inspired thermal spreader. In the first budget period, we developed a new concept and corresponding material structure that breaks the limit of phase-change heat transfer (Leidenfrost limit). The developed concept, decoupled hierarchical structures, is implemented in both Si and Cu structures. In the second budget period, we studied fundamentals of liquid-vapor phase change in a controlled evaporation chamber to tune and measure interfacial mass and heat transfer at an evaporating interface. We formed a *predictive model* based on the non-equilibrium thermodynamics that can predict mass and energy flux independently. In contrast with the current gas kinetics models, the developed model satisfies both momentum and energy conservations. This model provides groundwork for all the liquid-vapor phase-change studies. In the other task of this research program, we studied limits of evaporative heat flux in nano-confined geometries. We studied thin-film evaporation in nanochannels under absolute negative pressure in both transient and steady-state conditions. The findings suggest that thin-film evaporation in nanochannels can be a bubble-free process even at temperatures higher than boiling temperature providing high reliability of thermal management systems. To achieve this bubble-free characteristic, the dimension of nanochannels should be smaller than critical nucleolus dimension. In steady-state condition, unprecedented heat flux of **14274** Wcm$^{-2}$ is achieved in the nanochannels, which corresponds to liquid velocity of 0.26 ms$^{-1}$. This ultra-high heat flux is demonstrated for a long-time period. The developed structure provides a rational route to design thermal management technologies for high-performance electronic/photonic devices.

In the third budget period, we studied interfacial phenomena at Knudsen layer adjacent to liquid-vapor interface. We solved Boltzmann Transport Equation (BTE) through Mont-Carlo simulation of vapor phase at the liquid-vapor interface. These simulations provided a molecular-scale insight on physical phenomena occurring at liquid-vapor interface. The determined temperature profile in Knudsen layer by these simulations addressed the *long-debated* temperature discontinuity at the liquid-vapor interface. Despite measured temperature discontinuity up to 15 $^{o}$C at evaporating interface of liquid-vapor, we proved that the measured discontinuity is a function of vapor boundary condition and *is not an intrinsic characteristic of liquid-vapor interface*. This finding closes the discussion on the correct thermodynamic boundary conditions needed to be used to determine kinetics of evaporation. As we have a plan to achieve extreme heat fluxes close to kinetics limit, we tried to eliminate momentum limit of liquid transport through slip boundary condition at solid-liquid interface. Through a well-customized approach, we grafted monolayer of Graphene on nanochannels. The slip boundary condition imposed by Graphene resulted in an order of magnitude higher mass flux in the nanochannels. This higher mass flux provided a route to boost heat dissipation capacity of nanochannels and develop heat spreaders for extreme environments.

### Research Tasks

Miniaturization has been the hallmark of electronic and photonic instruments in the last few decades. The miniaturization efforts span in an enormous range of dimension from nanoscale transistors to thumbnail- sized chips, smartphone, vehicle electronic and server farms. This miniaturization accompanied by enhanced functional density necessitates enhanced heat dissipation, which has been the bottleneck of further advancement in these technologies. The current CPU power densities have reached to several hundred Watt per square centimeter. This constantly growing CPU power density has introduced a high demand for advanced cooling systems. A range of approaches has been studied to address this high heat dissipation challenge including jet impingement, sprays, and micro-channels. However, thin film evaporation with nanometer fluid thickness is considered as one of the most promising approaches to address the future demands. Although addressing space-averaged heat flux in electronic components is one aspect of the heat management, instantaneous local hot spots are mostly the main source of failure in the electronic/photonic devices. In other words, the instantaneous local high heat fluxes above the cooling limit of the heat dissipation system cannot be accommodated by the system and cause the failure. Most of the studies in the heat dissipation by thin film evaporation are focused on steady-state operation and are aimed to boost the space-averaged dissipated heat flux. However, addressing the transient hot spots remains to be an open challenge. Here, we present a new idea inspired by transpiration system in the plants to develop smart thermal spreaders that can both manage the high heat flux and accommodate the instantaneous local hot spots. This new thermal spreader accommodates the instantaneous local hot spots in a smart fashion with no need for external control. The research program herein will be launched by fundamental studies of thin film evaporation in the nano-pores through a unique platform.

## Research Tasks

### Task 1: Experimental Study of Evaporation in Nano-Scale Confinements

Miniaturization has been the hallmark of electronic and photonic instruments in the last few decades. The miniaturization efforts span in an enormous range of dimension from nanoscale transistors to thumbnail-sized chips, smartphone, vehicle electronic and server farms. This miniaturization accompanied by enhanced functional density necessitates enhanced heat dissipation, which has been the bottleneck of further advancement in these technologies[12]. The current CPU power densities have reached to several hundred Watt per square centimeter. This constantly growing CPU power density has introduced a high demand for advanced cooling systems[13]. A range of approaches has been studied to address this high heat dissipation challenge including jet impingement[14], sprays[15] and micro-channels[16,17]. However, thin film evaporation with nanometer fluid thickness is considered as one of the most promising approaches to address the future technological demands[18–30]. The thickness of liquid film in this phenomenon should be in nanometer scale to reduce thermal resistance for heat transfer. Thin film evaporation phenomenon in micro/nanostructures is a coupled multi-physics momentum transport, energy transport, and gas kinetics problem. The momentum transport governs the liquid flow to the liquid-vapor interface; the energy transport governs the heat transfer to the interface, and the gas kinetics governs the evolution of molecules from liquid phase to the vapor phase. Depending on time scale, length scale, and the thermodynamic properties of the liquid-vapor interface, each of these physics imposes a limit on the kinetics of thin film evaporation. On the momentum transport aspect, miniaturization of the electronic devices and consequent cooling systems increases hydraulic resistance of the fluid flow. As the radius of confinement for the fluid flow decreases, the fluid transport to the liquid-vapor interface becomes limited. On the energy transport aspect, the energy transport to the liquid-vapor interface is a function of solid-liquid thermal conductance, liquid-vapor thermal conductance and thermal diffusivity of the thin film of liquid. The dimension of nanostructures falls below the critical dimension of structure is defined as $L_c = \frac{C_L\, k_L}{G\, C_s}$, where $C_L$ denotes heat capacity of liquid, $k_L$ is the liquid thermal conductivity, $G$ is the thermal conductance of liquid-vapor interface and $C_s$ heat capacity of solid. For metal-water interfaces, G is in order of 100 $MWm^{-2}K^{-1}$ and $L_c$ will be in order of 30 nm. Thus, if the length scale of solid structures falls below this critical length scale, the role of interfacial energy transport becomes important and will appear in thermal management picture. On the gas kinetics aspect, thin film evaporative mass flux is limited by the net flux of molecules from the liquid-vapor interface to the vapor phase. Currently, there are three main theories on the evaporation phenomenon; Hertz-Knudsen model[31,32] (HK), Statistical rate Theory (SRT) and Non-equilibrium thermodynamics (NET). Summary of these theories are discussed above. As shown by Plawsky et al. the predicted limit of heat flux through kinetic theory is in order of $10^5$ $Wcm^{-2}$. Furthermore, the molecular simulations by Maroo and Chung[33] shows the same order of $10^5$ $Wcm^{-2}$ of gas kinetics limit which is far from the limit of current technologies. Thus, the current limit of thin-film evaporation is imposed by momentum transport.

Early in the development of micro/nanostructures for thin film evaporation, research studies only focused on transcending the momentum transport limit by optimizing geometry of micro/nanostructure of the thermal spreader. These include superhydrophilic micro and nanostructures such as micro-pillar arrays[34–37], copper micro-posts[38], sintered wick microstructures[39], multi-artery[40,41], and carbon nanotubes[42,43] to transport the liquid via capillary force. In capillary-driven fluid flow, the capillary pressure and viscous pressure are coupled to each other. As we move to smaller pore radius, the hydraulic resistance increases and eventually fluid flow will stop. Thus, the maximum liquid flow rate with optimized geometry on the micrometer scale is limited with capillary pressure on the order of 10 kPa. However, development of bi-porous approach[44–51] allowed to raise the limit imposed by the momentum transport. In this approach, the viscous pressure of fluid flow is divided in two parts, (I) the long length of fluid flow occurs in micro-channels with small hydraulic resistance (II) the short length of fluid flow occurs in the nanochannels with high hydraulic resistance. Thus, the overall small hydraulic resistance allows raising the limit of heat flux imposed by the momentum transport. The calculations by Xia et al.[45] shows that with 1 μm length scale of fluid flow in nano-membrane with porosity of 24%, interfacial heat flux in the value of 5000 $Wcm^{-2}$ could be achieved. In another interesting work, Li et al.[52] explored limits of evaporation in nanoscale conduits. Capillary driven-evaporation was conducted at the mouth of nanochannels. The studied structure was composed of a nanochannel with a step in height. The capillary pressure gradient between two sections with different heights transported liquid from the larger side to the smaller side for evaporation. By probing the motion of liquid in the large channel, evaporation rate in the smaller channel was extracted. The authors found a kinetic limit of evaporation at the mouth of nanopores. This limit was independent of outward diffusion of vapor molecules. In contrast with other predictions, they suggested that this limit ~ 8500 $Wcm^{-2}$ corresponding to flow velocity of 0.04 $ms^{-1}$ is imposed by kinetics of molecules motion form liquid to vapor phase. In addition, they suggested that value of evaporation coefficient of Hertz-Knudsen model can be higher than 1. In another study, by Radha et al.[53] limits of capillary evaporation in nanochannels with height in the range of angstrom is explored. A multi-layer of Graphene is used to develop these nanochannels. With water contact angle of 55-85$^o$ on these Graphene sheets, flow velocity of 0.1 $ms^{-1}$ was achieved. The authors found that momentum transport is the limiting factor nor diffusion and kinetics of liquid molecules transformation to vapor phase. Although great strides have been made to achieve higher limits, much work remains to be done to reach gas kinetics limit of evaporation.

Here, we utilized concept of liquid absolute negative pressure in nanochannels to achieve unprecedented heat fluxes through thin-film evaporation. For a curved interface, Yonge-Laplace equation governs pressure discontinuity across the interface and is written as $P^V - P^L = \sigma^{LV}(C_1 + C_2) + \Pi$, where $P^L$ denotes the liquid pressure, $P^V$ is a vapor pressure, $\sigma$ is a liquid-vapor surface tension, and $C_1$ and $C_2$ are two principals curvatures of the interface and $\Pi$ is a disjoining pressure. The disjoining pressure that describes the water-surface interaction dominates at scales < 100 nm[54], but rapidly decrease at larger scale. For a hydrophilic solid-liquid-vapor combination, as the curvature of a liquid-vapor interface increases, the liquid can adopt negative absolute pressure.

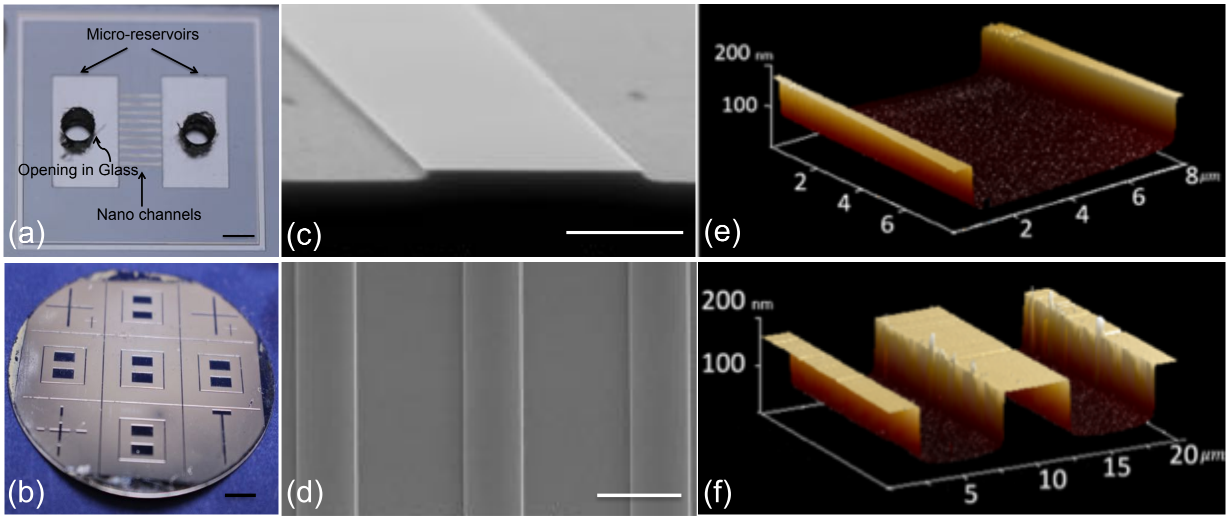

**Figure 4.** a) Developed nanochannels and micro-reservoirs on Si wafer after anodic bonding. The whole structure is sealed with borosilicate glass. There are two holes in the glass to facilitate the fluid introduction. The scale bar is 1mm. b) five sets of channels developed on 2 inches Si wafer. The scale bar is 5mm. c) SEM image of the nanochannels, tilted along the axis perpendicular to the width-height plane with a tilt angle of 45°. The scale bar is 2 μm. d) The top view SEM image of two individual nanochannels. The scale bar is 5 mm. AFM characterization of e) one individual nanochannel f) two nanochannels before anodic bonding indicating the uniformity and accurate dimension of channels.

That is, the liquid is under a tension, which is a metastable thermodynamic state, but stable mechanical state ($\frac{\partial P}{\partial V} < 0$). At centerline of the liquid-vapor interface, the principle curvatures are written as $C = \cos\theta / r$, where $\theta$ represents the contact angle and $r$ the radius of a confinement. High curvature interfaces can be developed in nanoconfined geometries (e.g. small $r$). The negative pressure at the liquid-vapor interface provides a substantial driving force for liquid flow to the interface for evaporation, which raises the limit of momentum transport. Here, we studied both transient and steady-state characteristics of thin-film evaporation under negative pressure in nanoconfined geometries and demonstrated that heat flux in order of 14 ± 1 $\text{kWcm}^{-2}$ is achieved in steady-state condition.

To achieve negative pressure at the liquid-vapor interface, we fabricated an array of closed nanochannels as shown in **Fig. 4a**. The fabrication processes were conducted on a 2 inches-diameter and 0.3 μm thick silicon wafer with photolithography, two steps of reactive ion-etching and anodic bonding. In the first step, the positive photoresist (AZ1512) was coated on the silicon wafer using a spin coater (Brewer Cee 200 Spin Coater) in order to reach 2 μm thickness (figure S1.b). The geometric pattern was designed on solid works and transferred on to a 4 inches chrome mask with a resolution of 1 μm. The optical mask was used to pattern the photoresist through exposing it to UV irradiation (ABM Mask Aligner. Then the sample was immersed in AZ-300 developer, washed with deionized water and dried with Nitrogen flow. The nano-channel patterns were etched into the silicon wafer using reactive ion etching (Oxford Plasma Lab ICP 180 RIE). The sample was washed with acetone, alcohol, deionized water and subsequently dried with Nitrogen flow. All the steps including spin coating and photolithography were repeated to make the micro-reservoir patterns. The micro-reservoir patterns were etched deeper by enhancing the etching power and time. These micro-reservoirs pump the fluid to the channels via capillary force for evaporation. Borosilicate glass with a thickness of 1.1 mm was used to seal the channels through anodic bonding (AML AWB-04 Aligner Wafer Bonder). Initially, two holes were drilled on the glass in order to facilitate the introduction of the fluid to the micro-reservoirs. Next, the silicon wafer and borosilicate glass were dipped into piranha solution ($H_2SO_4$: $H_2O_2$=3:1) for 15 min. After cleaning, the silicon wafer and borosilicate glass were bonded together by the anodic bonding process carried out for 10 min at 400 $^{o}$C with a voltage of 700 V.

The developed structure is made up of 9 sets of nanochannels and two micro-reservoirs placed perpendicularly along the two ends of the nanochannels. Each set of nanochannels consists of 11 separate channels with width of 6 μm, depth of 180 nm and length of 1.6 mm. The reservoirs are 2 mm in width, 4 mm in length and 25 μm in depth. These micro-reservoirs pump the liquid to the channels via capillary force for evaporation. We developed five sets of channels in each Si wafer, **Fig. 4b** to boost the number of samples and reduce error in our measurements. The geometry of the channels was examined with Scanning Probe Microscopy (SPM) and Scanning Electron Microscopy (SEM), as shown in **Fig. 4c-4f,** respectively. As shown, the developed channels are highly uniform and consistent. This consistency allows us to have a sound interpretation of the experimental results. Borosilicate glass with a thickness of 1.1 mm was used to seal the channels through anodic bonding. The developed nanochannels were cleaned thoroughly before the experiments through plasma cleaning. We chose isopropyl alcohol as the working liquid in all experiments as it provides complete wettability of Si nanochannels and contact angle close to zero.

A schematic of an evaporating interface inside a 2D nanochannel is shown in **Figure 5**. As shown, $\cos\theta = \frac{r}{R}$ and $\sin\theta = 1 - \frac{h}{R}$, one can find $\frac{h}{r} = \frac{1-\sin\theta}{\cos\theta}$. Therefore, by measurement of $\frac{h}{r}$, contact angle can be determined.

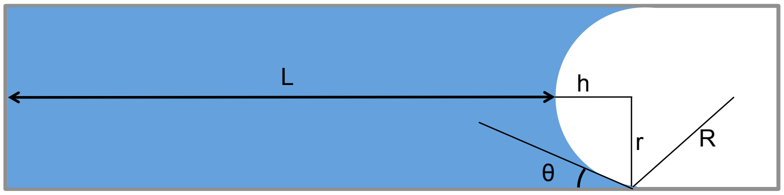

**Figure 5.** Schematic of liquid-vapor interface inside a 2D nanochannels. θ denotes a contact angle, r is the dimension of nanochannels, h is the centerline depth, and L is the liquid phase length.

The liquid-vapor interface for one set of nanochannels is shown in **Figure 6**. The values of h and r were measured through image processing and the values of contact angles in the nanochannels are presented in **Table 3.**

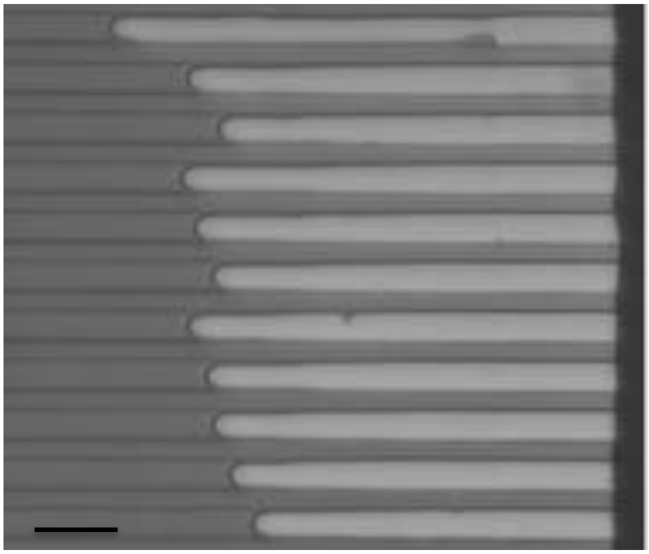

**Figure 6.** One set of nanochannels used to measure contact angle. Channel 1 is a first channel from the top. The scale bar is 20μm.

**Table 3.** Contact angle for one set of nanochannels

| **nanochannel** | **r (μm)** | **h (μm)** | **h/r** | **θ ($^o$)** |
|---|---|---|---|---|
| 1 | 2.25 | 2 | 0.888 | 6.66 |
| 2 | 2.3 | 2.2 | 0.956 | 2.34 |
| 3 | 2.3 | 2.1 | 0.913 | 5.39 |
| 4 | 2.4 | 2.2 | 0.916 | 4.77 |
| 5 | 2.4 | 2.2 | 0.916 | 4.77 |
| 6 | 2.35 | 2.3 | 0.978 | 1.15 |
| 7 | 2.4 | 2.3 | 0.958 | 2.34 |
| 8 | 2.5 | 2.3 | 0.920 | 4.77 |
| 9 | 2.5 | 2.4 | 0.960 | 2.34 |
| 10 | 2.45 | 2.2 | 0.897 | 6.02 |
| 11 | 2.4 | 2.3 | 0.958 | 2.34 |

Two length scales should be considered in the nanochannels, to determine principle curvatures, width and depth. Considering these scales, the liquid pressure at the liquid-vapor meniscus is -158.5- -90.4 kPa. The liquid pressure at liquid vapor interface is calculated through Young-Laplace equation, $\Delta p = \sigma C$, where $\Delta p = p_v - p_l$ is a pressure discontinuity across the liquid vapor interface. $p_v$ denotes the vapor pressure and is equal to $p_{atm} \cong 10^5\ Pa$, $P_{\square}$ is a liquid pressure, $\sigma$ is surface tension of the liquid and $C$ is a curvature of the liquid-vapor interface which can be expressed as $C = \frac{1}{R_1} + \frac{1}{R_2}$, where $R_1 = 90\ nm$ is half of the channel's height and

$R_2 = 3\ \mu m$ is half of the channel's width. Taking the dependence of surface tension on temperature, liquid pressure at different temperatures is determined and tabulated in **Table 4**.

**Table 4.** Surface tension, liquid pressure and critical radius of bubble nucleation at various temperatures.

| **Temperature (°C)** | $\boldsymbol{\sigma\ (\frac{mN}{m})}$ | $\boldsymbol{P_l\ (k\,Pa)}$ | $\boldsymbol{R_C\ (nm)}$ |
|---|---|---|---|
| 25 | 22.6 | -158.5 | 275 |
| 38 | 21.6 | -146.9 | 268 |
| 55 | 20.2 | -130.7 | 250 |
| 70 | 19 | -116.6 | 214 |
| 75 | 18.7 | -113.7 | 198 |
| 80 | 18.3 | -108.6 | 183 |
| 85 | 17.9 | -104 | 166 |
| 90 | 17.5 | -99.5 | 150 |
| 95 | 17 | -93.8 | 133 |
| 100 | 16.7 | -90.4 | 118 |

Once the nanochannels are developed, we studied thin film evaporation under negative pressure in two regimes: (1) Transient evaporation and (2) Steady-state evaporation.

The schematic of experimental setup for transient and steady state experiments are shown in **Fig. 7a, 7b,** respectively. Note that in the steady state experiment a droplet of working fluid on the cold micro-reservoir constantly provides liquid for evaporation. The evaporation experiments were conducted at isothermal condition for transient evaporation and locally heated conditions for steady state evaporation. The experimental set-up for isothermal evaporation experiment can be observed in **Fig. 7a.** Silicon rubber heater (Omega, SRFG-101/10-P), connected to a DC power supply, was used as a heater in all experiments. Isothermal evaporation experiments were performed at different temperatures (ranging from 25°C to 100°C). Temperature was measured through the K-type thermocouple connected to the thermometer. The thermocouple was fixed on the silicon wafer using a thermal paste. The developed nanofluidic device was cleaned through plasma cleaning before each set of experiment to avoid any contamination, and then it was filled with isopropyl alcohol and installed on top of the heater. It should be mention that one thick insulator layer (Buna-N/PVC foam) was put underneath of the heater to reduce the heat loss. The outlet of one micro channel was covered by tape in order to suppress the evaporation at that reservoir. Therefore, evaporation took place faster at uncovered micro reservoir and continued to the nanochannels from one side till it dried out completely. Initiating evaporation from one side at nanochannels enabled us to precisely track the liquid vapor interface. A high-speed camera (AMETEK, VR0315, 70 frames per second) connected to the optical microscope (Nikon, ECLIPSE LV100ND) was used to monitor the liquid vapor interface movement. The experimental set-up for locally heated evaporation experiment is presented in **Fig.7b**. The set-up is almost the same as the isothermal evaporation experiment. The only difference is that in this experiment the chiller was paired to the heater to cause the temperature difference across the nanochannels to obtain the steady state of evaporation. It should be mention that during the experiment, a droplet of IPA was placed on the outlet of the cold reservoir to make sure sufficient supply of liquid to the interface is provided.

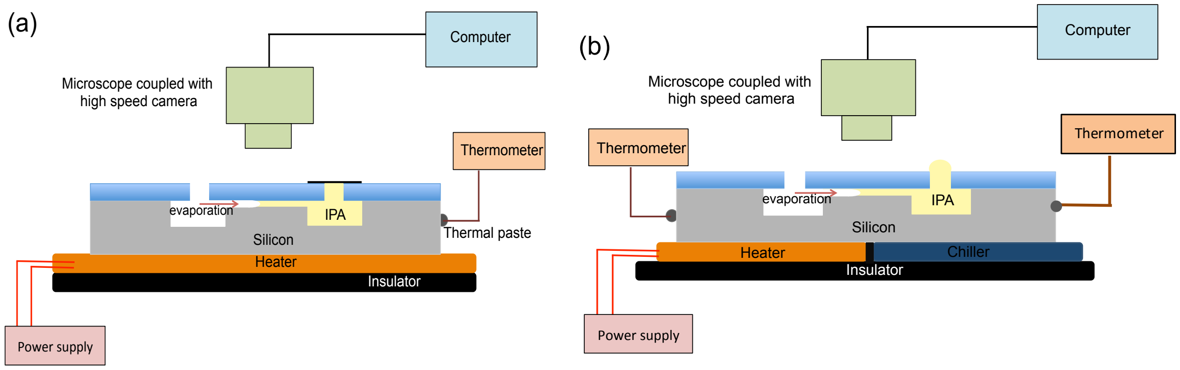

**Figure 7.** Schematic of experimental set-up a) for a transient thin film evaporation in nanochannels. b) for a steady state thin film evaporation.

In transient experiments, we studied motion of liquid-vapor interface in a nanoconfined geometry. Initially, working fluid was introduced from one micro-reservoir to completely fill the channels and the other micro-reservoir. The nanochannels were examined under an optical microscope (Nikon, ECLIPSE LV100ND) to ensure no trapped air bubbles in the channels. The experimental setup is placed on an isothermal platform with temperature varying between 25°C to 100°C. Since one of the micro-reservoirs were sealed, the evaporation initiated from the other reservoir and continued in the channel up to reaching the other reservoir. The motion of liquid-vapor interface was probed through high-speed imaging (Phantom 711, vision research) coupled with the optical microscope. **Figure 8** shows the isothermal evaporation in nanochannels at 55°C, 75°C and 95°C at different times. The liquid phase looks dark while the vapor phase is the brighter stream. The remarkable aspect of these experiments is absence of any bubble in the channels at temperatures more than the boiling temperature of the working liquid (i.e. isopropyl alcohol) at ambient pressure, which is ~ 83 $^{o}$C. Although we were expecting to move from thin-film evaporation regime to nucleate boiling at higher temperatures than boiling temperature, we did not observe any bubble formation. Note that the liquid in the nanochannels is at lower pressure than atmospheric pressure resulting in lower boiling temperature according to Clausius-Clapeyron equation. Formation of bubble in channels leads to instabilities, back flow and formation of hot spots and consequently is undesirable in thermal management devices. The fundamental underpinning of this exciting feature comes from thermodynamics of bubble formation. In a liquid-vapor system, a nucleus of vapor/gas should adopt a critical radius before further growth. The critical radius of spherical bubble ($R_c$) is written as

$$R_c = \frac{2\,\sigma^{LV}}{P_s \exp\left(\frac{v_l}{RT}\left(P^L - P_s\right)\right) - P^L} \tag{4}$$

where $v_L$ denotes specific volume of the liquid and $P_s$ is the saturation pressure. For the given thermodynamic state of liquid in the nanochannels, the minimum critical radius of spherical bubble is ~183 nm. This length scale is more than the depth of nanochannels. That is, if a vapor nucleus forms in the nanochannels, it cannot adopt the critical radius and grow further. Thus, the minimization of energy (i.e. maximum entropy principle) requires the vapor nucleolus collapse. Although the length scale in width dimension of nanochannels is more than the critical nucleolus dimension, formation of stable ellipsoid vapor/gas bubble was not observed. We conducted more than 20 experiments at temperatures higher than boiling temperature and no bubble formation was observed. This fact is also shown by molecular dynamic simulations of Maroo and Chung[55]. This suggests that we can keep thin-film evaporation in nanochannels even at high temperatures.

Through image analysis, we determined transient coordinate of liquid-vapor interface for three nanochannels as shown in **Fig. 9a-9c**. The corresponding velocity in these channels as a function of temperature is determined as shown in **Fig. 9d**. The uniform dimension of nanochannels and isothermal condition provide a consistent average velocity for all the studied channels.

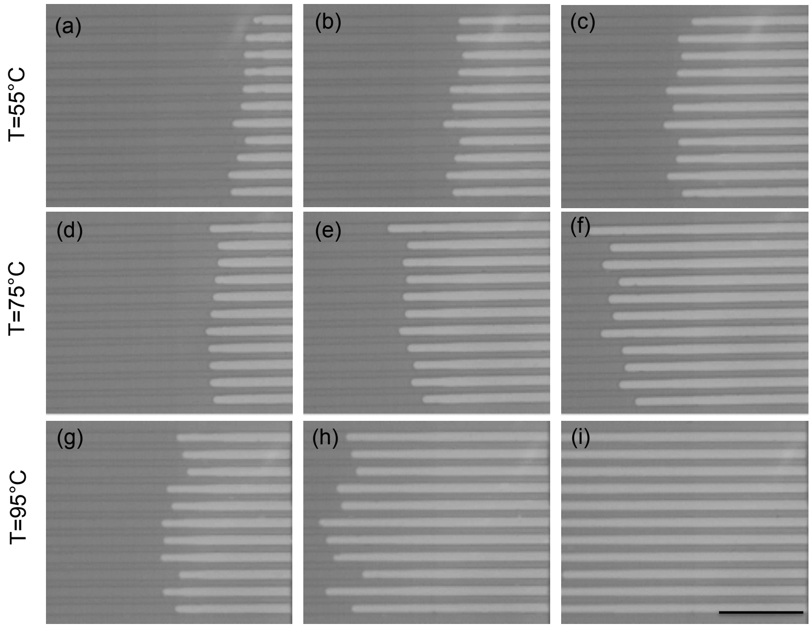

**Figure 8.** The isothermal evaporation at nanochannels is probed using a high-speed camera to determine the average velocity of interface and determine the local heat flux. (a), (b) and (c) show the isothermal evaporation experiment performed at 55°(d), (e) and (f) at 75°C, and (g), (h) and (i) at 95°C, for 0.41s, 0.82s and 1.24s after beginning the evaporation at nanochannels, respectively. No bubble formation was observed at 95°C which is higher than boiling temperature of IPA. The scale bar is 50 μm.

The velocity of receding liquid-vapor interface increases monotonically with temperature and interestingly reaches a plateau at high temperatures. No further increase in temperature affects the velocity of receding interface. Note that although temperature of substrate is higher than boiling temperature in some cases, the liquid remains at saturation temperature during evaporation. Furthermore, corresponding interfacial heat flux at these nanochannels is shown in **Fig. 9e**. The fundamental question is how fast an evaporating liquid-vapor interface could move in nanochannels.

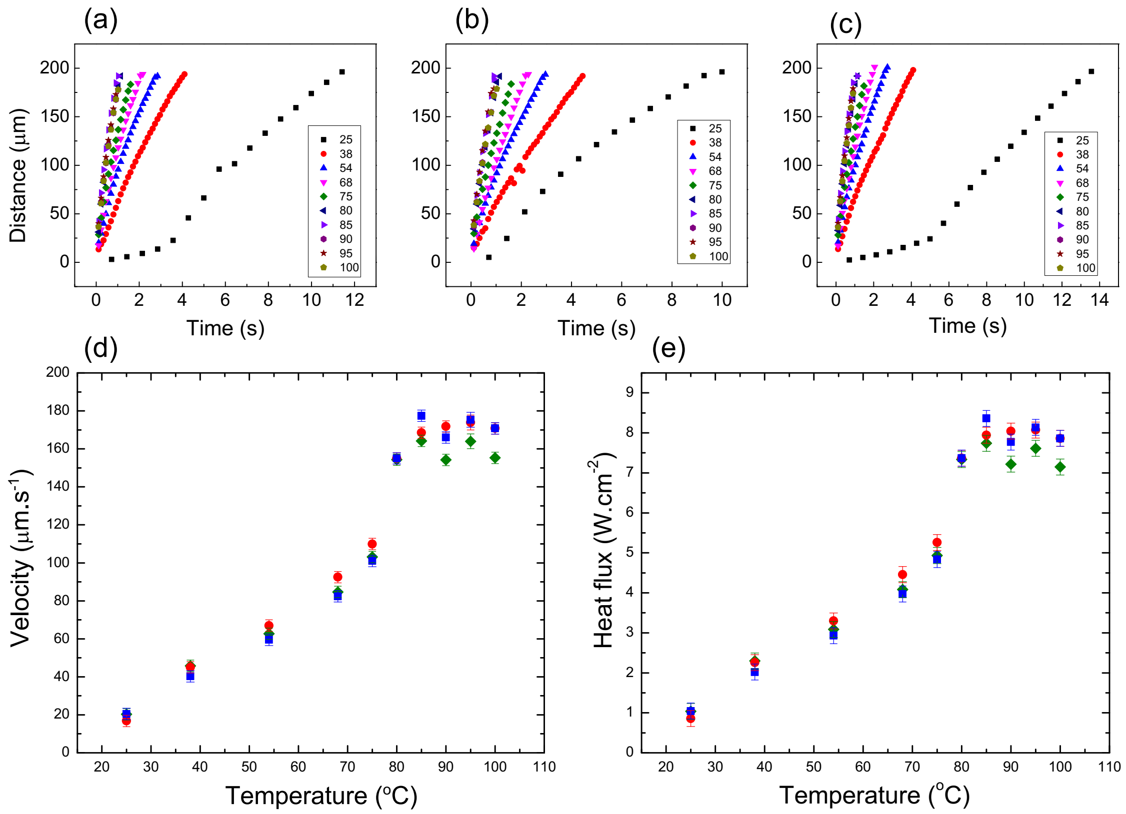

**Figure 9.** a), b) and c) Liquid vapor interface as a function of time for three individual channels at different temperatures ranging from 25 to 100°C. d) The average velocity of liquid-vapor interface as a function of temperature for three individual channels. The velocity increases as temperature increases and reaches a plateau at higher temperatures. e) The corresponding local heat flux as a function of temperature.

This phenomenon can be realized through fundamental of thin film evaporation and fluid dynamics of an evaporating liquid-vapor interface. Thin film evaporation should be viewed in the context of an evaporating meniscus, which can be divided into three regions including bulk meniscus, transition region and an adsorbed film, **Fig. 10**. Theories on thin-film evaporation suggest diverging evaporative flux in the transition region. This fact is shown both for diffusion-limited evaporation discussed by Hu and Larson[56] (valid for low evaporation fluxes) and energy approach discussed by Ghasemi and Ward[57,58]. That means the evaporation flux along the liquid-vapor interface is not uniform. The diverging local evaporation flux in a transition region requires liquid flow to this region from the bulk meniscus region. Otherwise, the high evaporation flux in the transition region changes the contact angle close to π/2, which is not in agreement with the measurements. The contact angle of liquid in nanochannels is always below π/2 and could change between 2-7°. For the liquid flow from the bulk meniscus to the transition region for constant contact angle, the viscous dissipation (FV) should be balanced by the applied momentum on the liquid-vapor interface. Through analysis of this balance, one finds that average velocity of liquid-vapor interface is written as $V = \frac{\sigma}{6\,\mu \ln(\frac{r}{a})}\,\theta_D\,({\theta_D}^2 - {\theta_e}^2)$, where $\mu$ denotes dynamic viscosity, $a$ thickness of adsorbed film, $\theta_D$ dynamic contact angle, and $\theta_e$ equilibrium contact angle. This velocity form has two consequences. For $\theta_D = \theta_e$, velocity of liquid-vapor interface is zero. That is, no imposed force on the contact line (i.e. no evaporation and no induced recoil pressure). By increasing the evaporation flux and corresponding recoil force, the velocity of liquid-vapor interface increases and reaches a maximum corresponding to $V_m = \frac{\sigma}{9\sqrt{3}\,\mu\ln(\frac{r}{a})}\,\theta_e{}^3$, (i.e. $dV/d\theta_D = 0$). For low values of $\theta_D$ velocity of liquid-vapor interface drops. That is, at highly sharp-edged liquid-vapor interface, viscous dissipation of liquid flow to the transition region is so high and does not allow sufficient fluid flow to transition region for evaporation. Looking back at the experimental results suggest that at low temperatures, the contact line velocity is monotonically increases with temperature. However, at high temperature, the contact line attains a maximum velocity as discussed and any further increase in the temperature of substrate does not affect the velocity of interface. The maximum velocity of contact line is 160-180 μms$^{-1}$. If one includes this velocity range in the maximum velocity formulation, we attain equilibrium contact angle of 4$^{\circ}$, which is completely consistent with the measured contact angles (i.e. 2-7$^{\circ}$).

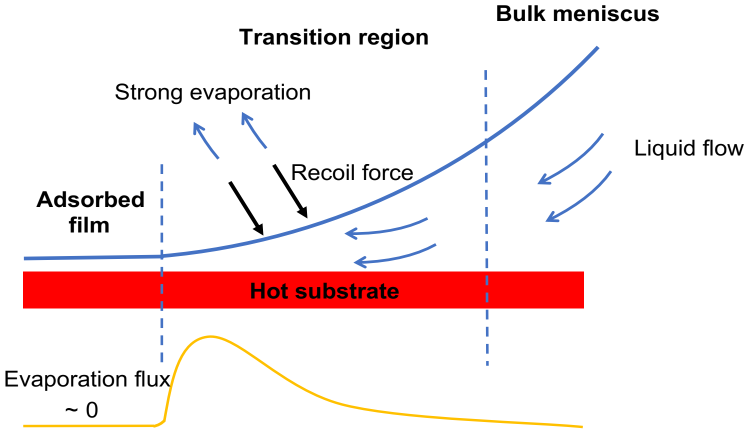

**Figure 10:** A schematic of profile of liquid-vapor interface. High evaporation flux in the transition region leads to strong recoil pressure and change of local contact angle.

This suggests that dynamic of a contact line in the confined geometries is limited by viscous dissipation of liquid flow in the meniscus. The evaporative heat flux for the transient experiments is shown in **Fig. 9e**. The interfacial heat flux of a moving contact line is limited by liquid flow to transition region and cannot adopt high values. Higher limits of heat flux can be obtained for larger equilibrium contact angle. However, if a stationary contact line is achieved (i.e. steady-state condition), this limit of fluid flow to the transition region could be omitted and high heat fluxes can be achieved. We explored this characteristic in the next section.

The schematic of the setup for steady-state evaporation is shown in **Fig. 11**. The objective in these studies is to explore limits of thin-film evaporation under negative absolute pressure. As shown, the micro-reservoirs are kept at two different temperatures. Initially, working fluid was introduced from one micro-reservoir to completely fill the channels and the other micro-reservoir. The nanochannels were examined under an optic al microscope to ensure no trapped air bubbles in the channels. A chiller and a heater were paired and put underneath of the structure to provide a temperature difference across the structure. An insulating layer was used to separate the chiller and heater. The chiller was located under the cold reservoir, while the heater was located under hot reservoir. The chiller's temperature was kept fixed at 16 °C and the heater temperature was adjusted at three different temperatures including 20 °C, 40 °C and 60 °C. Once the temperature field is imposed, evaporation initiates from the hot reservoir until the reservoir is depleted. Then, the evaporating interface moves in the nanochannels.

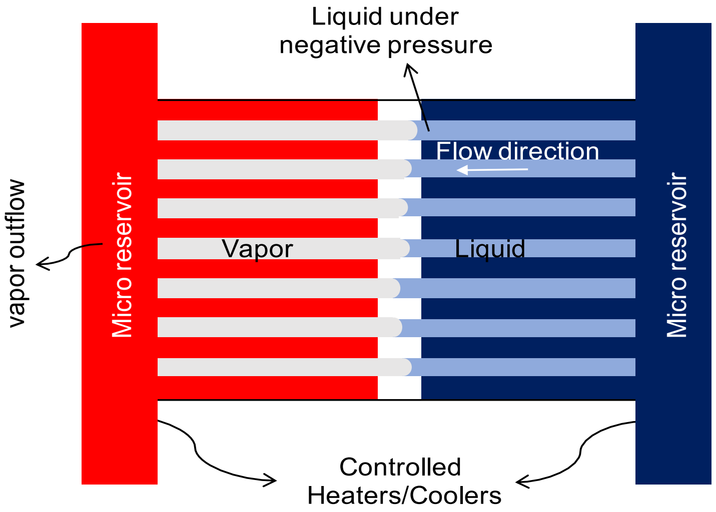

**Figure 11:** Schematic of the locally heated evaporation experiment to explore the maximum evaporation heat flux is shown. Evaporation takes place from the hot micro-reservoir and continues to the nanochannels.

The coordinate of liquid-vapor interface in the nanochannels were visualized by the optical microscope. **Figure 12** shows the motion of liquid-vapor interface at hot reservoir temperature of 40°C at various times. The length of liquid phase at nanochannels decreases until it reaches to a specific coordinate with no further motion. At this specific coordinate, the capillary pumping of fluid by the cold reservoir is balanced by the evaporating mass flux at the liquid-vapor interface and a steady-state evaporating condition is achieved. We should emphasize that the cold reservoir is completely filled with the working fluid and a droplet of fluid is sitting on the cold reservoir to ensure sufficient supply of liquid to the interfaces. The fluid in the cold reservoir is at ambient pressure, while the liquid at the liquid-vapor interface experience negative absolute pressure. To ensure the steady-state condition, we recorded the coordinate of liquid-vapor interface for more than 3 minutes and no further motion was observed. Given the length of the liquid in the nanochannels, the local heat flux at the interface is written as[59]

$$\dot{q} = \frac{\rho\, h^2\, \Delta P\, h_{fg}}{12\, \mu\, L} \tag{5}$$

The determined heat fluxes as a function of length of fluid in the nanochannels is shown in **Fig. 13**. At each hot reservoir temperature, the evaporation heat flux shows the inverse trend with the liquid phase length. A maximum evaporation heat flux was obtained for a liquid stream with 3 ± 0.5μm length of liquid phase at 60 °C corresponding to a heat flux of 14 ± 1 kWcm$^{-2}$, which is extremely high among the heat fluxes reported so far[45],[52].

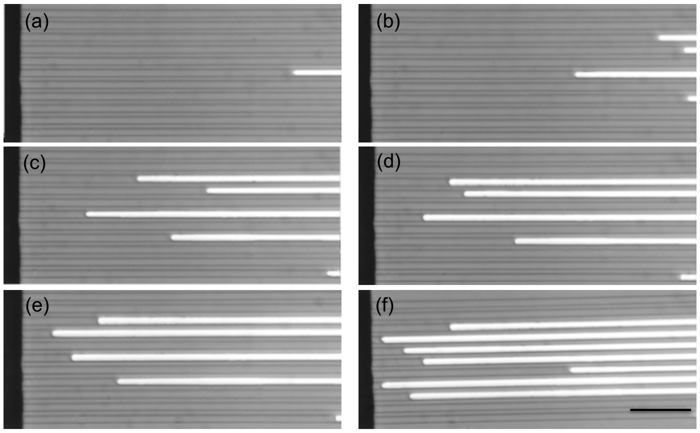

**Figure 12.** Microscopic images of a locally heated evaporation experiment performed at 40°C at different times are shown. Time increases from (a) to (f). The length of vapor phase (brighter area) increases as time goes on (from (a) to (e)), and reaches a steady state of evaporation in (f). The steady state of evaporation was obtained more than 10 minutes. The scale bar is 50 μm.

The negative absolute pressure of liquid and small length of fluid stream resulted to this high interfacial heat flux. Note that at these values of heat flux, even for all channels, it takes 45 min to evaporate the liquid droplet on top of cold reservoir.

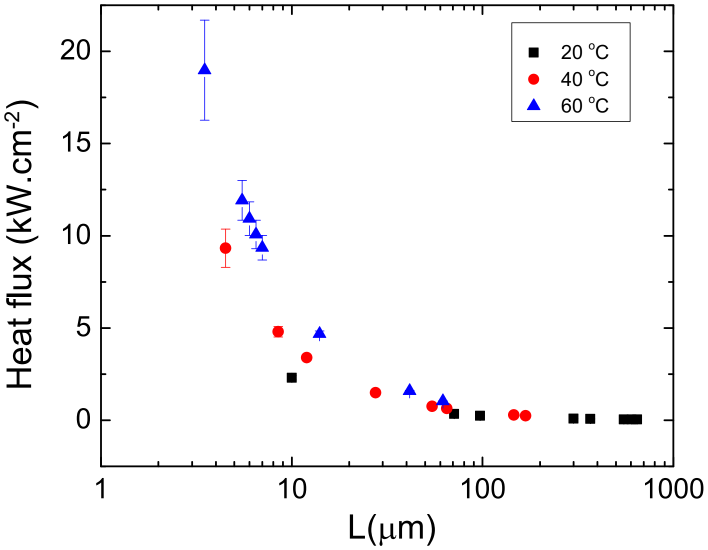

**Figure 13.** Evaporation heat flux as a function of liquid phase length in nanochannels at steady state of evaporation for different temperatures of hot reservoirs changing from 20°C to 60°C. The maximum evaporation heat flux obtained is 14274 W.cm$^{-2.}$

Once the vapor is generated, it should flow in the nanochannels and leave the structure through hot micro-reservoir. The Peclet number of vapor (convective transport to diffusion transport) is ~ 62000. For the vapor outward flow, we should initially determine which mechanism (advection or diffusion) is the dominant transport phenomena. The Knudsen number is written as

$$K_n = \frac{\lambda}{L} = \frac{k_B T}{\sqrt{2}\pi d^2 ph} \tag{6}$$

where $\lambda$ denote the molecular mean free path, $L$ is a physical length scale (in our case it is considered as channel's height), $k_b$ is the Boltzmann constant, T is the temperature, d is the diameter of vapor molecules and p is pressure. For isopropyl alcohol, $\lambda$ is 24 nm and $d$ is $6.5\times10^{-10}\ m$ and consequently Knudsen number is 0.135, which is in the range of 0.01 to 10. This indicates that the diffusion process is between Knudsen diffusion regime and molecular diffusion regime, and the diffusion coefficient inside the nanochannel is calculated from the Knudsen $(D_{kn} = \frac{h}{3}\sqrt{\frac{8RT}{\pi M_v}} = 0.204\, {cm^2}/{s})$ and molecular $(D_M = \frac{\lambda}{3}\sqrt{\frac{8RT}{\pi M_v}} = 0.028\, {cm^2}/{s}$ diffusion coefficient [ref-nanoletter]:

$$\frac{1}{\overline{D}} = \frac{1}{D_{Kn}} + \frac{1}{D_M} \tag{7}$$

Thus, the diffusion coefficient in the studied nanochannels is $0.024\, {cm^2}/{s}$. The relative ratio of advective transport to diffusive transport is written as

$$Pe = \frac{LV_v}{\overline{D}} \tag{8}$$

where L denotes the length scale (channel's length), $V_v$ is the vapor phase velocity. The velocity of the vapor phase is determined through conservation of mass at the liquid-vapor interface $\rho_L V_L = \rho_V V_V$. At the maximum evaporation flux, the velocity of vapor molecules is $93.14\, ms^{-1}$ considering $\rho_L = 748\, kgm^{-3}$, $v_l = 0.259\, ms^{-1}$ and $\rho_v = 2.08\, kgm^{-3}$. Thus, the Peclet number is 62093 which is >>1 indicating that vapor removal is governed by advection and diffusion does not play any role in vapor transport. This suggests that vapor transport is *not* diffusion limited and is driven by high inertia of vapor molecules. Also, as temperature of hot reservoir is more than saturation temperature of vapor, no condensation occurs in the nanochannels. At higher interfacial heat fluxes, steady-state condition could not be kept for more than 60 s as center of liquid-vapor interface enters the cold micro-reservoir. The findings suggest that higher heat fluxes are also possible by decreasing the length of nanochannels. Moreover, the momentum transport limit is still the physics of thin film evaporation.

Three transport phenomena are involved in evaporation at nanochannels including liquid transport to the liquid-vapor interface (Capillary-driven transport), interfacial phase-change of liquid to vapor phase (Gas kinetics transport), and vapor outward transport (advection and diffusion). Here, we compare the role of these transport phenomena in the evaporation through comparing resistance of each transport phenomena.

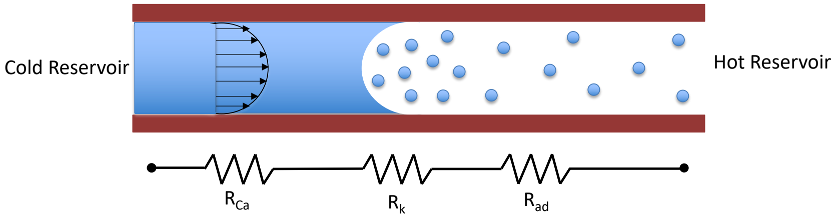

**Figure 14.** Resistance model for steady state evaporation

The corresponding resistance model can be observed in **Figure 14**. As it is shown, there are three major resistances in series inside the nanochannel. (i) The resistance of the liquid flow in the nanochannel can be written as $R_{Ca} = \frac{12\mu_l L_l}{h^2}$ ,where $\mu_l$ is a liquid viscosity, $L_l$ is a length of the liquid in the nanochannel, $\rho_l$ is a density of the liquid and h is a height of the nanochannels. (ii) The resistance of a phase change at the liquid-vapor interface is expressed as $R_k = \frac{\rho}{\sigma}\sqrt{\frac{2\pi RT}{M}}$, where $\sigma$ represents an empirical constant (considered 1), R is a universal gas constant and M is a molar mass of the fluid. (iii) for the vapor outward flow, as proved in the S8, it is dominant by advection. As a result, the resistance of the vapor flow inside the nanochannel is written as $R_{ad} = \frac{12\mu_g L_g}{h^2}$, where $\mu_g$ is a vapor viscosity, $l_g$ is a length of the vapor phase inside the nanochannel. The contribution of each resistance in the mass transport phenomena at steady state evaporation is demonstrated as percentage of the total resistance. The total resistance is equal to $R_{TOT} = R_{Ca} + R_k + R_{ad}$.The results indicate that the vapor flow (advection) resistance is a dominant resistance of mass transport at 60°C and even at 40°C. However, at 20 °C the capillary flow resistance becomes the dominating factor which is due to the higher length of the liquid phase at steady state evaporation compares to the higher temperature.

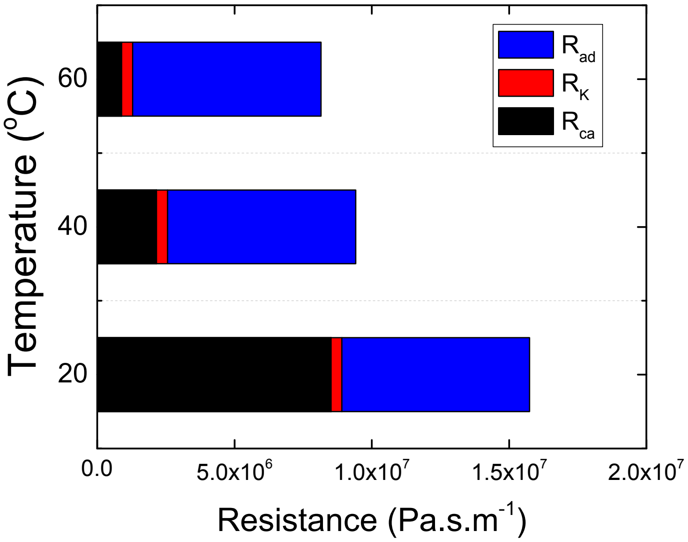

**Figure 15.** Contribution of different mass transport resistance is plotted at 20°C, 40°C and 60°C for the smallest length of liquid phase at each temperature. (i.e. 10 μm, 4.5 μm and 3μm for 20°C, 40°C and 60°C, respectively.) $R_{ad,}$ $R_k$ and $R_{Ca}$ present the advection resistance, phase change resistance and capillary flow resistance, respectively.

Also, we studied the implementation of these structures to break the limit of heat transfer, Leidenfrost limit. Evaporation and boiling are fundamental and core phenomena in a broad range of disciplines including power generation and refrigeration systems[1–9], desalination[10,11], distillation[12], electronic/photonic cooling[13–28], chemical reactors, aviation systems[29], and even biosciences[30–32]. Here, we are interested in cooling of a hot object through spray droplets[33,34].

Heat dissipation through direct contact of bulk liquid with a hot solid substrate (pool boiling) is extensively studied before[35–38] and still ongoing matter of study[39–41], but it is not focus of this work. Boiling heat transfer is characterized by the large dissipated heat flux for a small given superheat as it relies on the latent heat of the cooling fluid. Recently, Liang and Mudawar[42] reported a comprehensive review on the droplet phase change on heated walls. At low surface superheats, direct contact of the droplet with the solid substrate allows for very high heat dissipation capacity. However, at high surface superheats, formation of an insulating vapor layer at the solid-liquid interface limits the heat dissipation and the droplet levitates on a layer of vapor[43–50]. The onset temperature of this phenomenon is denoted by the Leidenfrost point (LFP)[51–56]. Under such conditions, the heat transfer rate is minimal and the temperature of the substrate can reach dangerous levels, such as those experienced in the Fukushima disaster. The limit of LFP has stalled abilities for thermal management of high-temperature devices and has impacted a broad spectrum of systems. The ability to raise LFP or to eliminate LFP opens a new path for breakthroughs in these systems.

A range of surface engineering approaches has been created to tune LFP. The earlier approaches included exploring different surface materials[57–59], tuning the roughness of surfaces[60–62], and using porous surfaces[63,64]. Recently, the dynamic field of nanotechnology has promised new avenues for surface engineering to tune LFP further. The later approaches included nanorough surfaces[9], nanofiber mats[65], micro/nano structured surfaces[66–73] and hierarchical surfaces[66,74]. In addition to surface engineering, other parameters such as tuning ambient pressure[75–77], chemical modification of the cooling medium[62,78–83], actuating inertia of the droplets[84–88] and active approaches (e.g. electrical fields[89–91]) are exploited to boost LFP. However, surface engineering is more appealing as other solutions are often constrained. We have summarized the reported LFP and their suggested physics for a water droplet with radius of 1.1-1.9 mm in **Table 1**. The maximum reported LFPs of a water droplet is for hierarchical structures in value of 453 $^{o}$C[74] and 400 $^{o}$C[66]. In both of these structures, micro-pillars of Si were coated with nanoparticles (NPs) to provide a multi-scale structure to boost LFP. Kim et al.[74] suggested a mechanism for superior performance of hierarchical structures. Once a droplet approaches a hierarchical surface, if the thickness of the features on the surface is less than the thickness of the insulating vapor film, the features will only increase the shear resistance for vapor flow and consequently thicken the vapor film. In this case, the surface features do not play any role in the increase of LFP. However, as the droplet evaporates, the thickness of Leidenfrost film decreases with the rate of $R^{4/3}$ [55] and the droplet ultimately forms contact with the surface. Note that $R$ denotes the radius of the droplet. Upon contact, the heterogeneous nucleation of bubbles can occur if cavities are available for nucleation. To introduce these cavities on the surface, Kim et al.[74] used nano-particles on the micro-posts of hierarchical structures to show the role of these nano-features on the transition from film boiling to nucleate boiling. Thus, both length scales on the surface contribute to boost LFP. Despite a long time effort, a rational approach for suppression of LFP is missing. This suppression will be a breakthrough in thermal management of high-temperature systems.

**Table 1.** The reported surfaces to boost LFP

| Approach | Fluid | Method | LFP limit ($^{o}$C) |
|---|---|---|---|
| Decoupled hierarchical structures (This work) | DI Water | Passive | No limit was found. |

| | | | |
|---|---|---|---|
| Hierarchical structures, Nano $SiO_2$ on Si posts[74] | DI Water | Passive | 453 |
| Hierarchical Si structure[66] | DI Water | Passive | 400 |
| Zirconium nanotube[92] | DI Water | Passive | 370 |
| Polymer nanofiber mats[65] | DI Water | Passive | 300 |
| Salt deposition on surface[83] | DI Water + KCl | Passive | 280 |
| Salts increased surface roughness[62] | DI Water + $MgSO_4$ | Passive | 240 |

In Leidenfrost phenomenon, the de-wetting upward force is caused by the pressure gradient of the vapor flow underneath of the droplet. This force keeps the cooling droplet suspended and impedes contact of the droplet with the hot solid substrate. Here, we have developed a new paradigm and corresponding material structure for suppression of Leidenfrost phenomenon. Through decoupled hierarchical structures, we re-route the vapor flow and keep the cooling droplet in contact with the hot solid at extremely high temperatures. These new structures are composed of two components, a nano-membrane and a deep microstructure, **Figure 5a**. Once a cooling droplet sits on the nano membrane, the generated vapor enters the deep microstructure and flows radially, while the nano membrane keeps the cooling droplet in contact with the hot solid through the capillary force. The de-wetting upward force by the vapor is only a function of dimensions of the microstructure, but downward capillary force, which keeps the droplet in contact with the hot solid, is only a function of pore dimensions in the nano membrane. As these forces are decoupled and independent, by tuning of these forces, the droplet can be kept in contact with the hot solid substrate even at high temperatures.

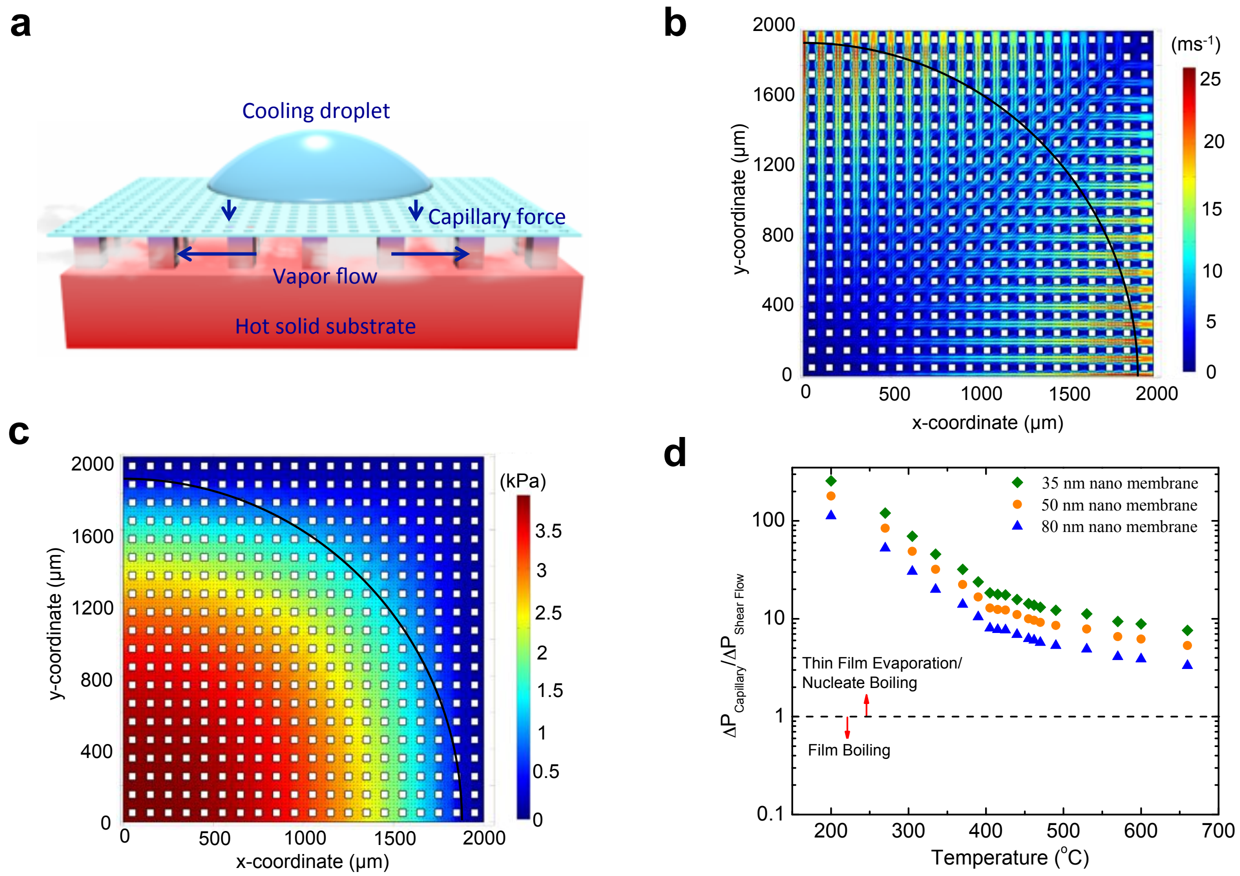

**Figure 5**. a) A schematic of decoupled hierarchical structure for suppression of Leidenfrost phenomenon is shown. The microstructure provides a path for generated vapor flow while the nano membrane keeps the cooling droplet attached to the structures. b) The velocity field in the microstructure is simulated at maximum measured heat flux of thin film evaporation (56.3 Wcm$^{-2}$). The white squares represent the micro-pillars, while the small black dots denote the pores of nano-membrane. The geometry of the nano-pores, dimension of microstructure, and the substrate temperature are the inputs to this model. The black line denotes the contact line of the cooling droplet. c) The de-wetting pressure field by the vapor flow is shown. This pressure should be lower than the capillary pressure by the nano-pores to keep the droplet attached to the structure. d) The ratio of de-wetting pressure to the capillary pressure as a function of temperature is shown. The onset of Leidenfrost phenomenon can be tuned with the dimension of nano-pores. For the pore radius of 80 nm, the Leidenfrost phenomenon is suppressed to more than 570 °C.

At Leidenfrost state, the insulating vapor layer impedes the direct contact of a cooling droplet and a hot substrate and significantly drops the dissipated heat flux. The thickness of static Leidenfrost film for small droplets is determined through the balance of interfacial mass flux and shear flow of vapor in the vapor film and is written as[52,55]

$$e = \left(\frac{k^v \, \Delta T \, \mu^v \, \rho_l \, g}{h_{fg} \, \rho_v \, \gamma^2}\right)^{1/3} R^{4/3} \qquad (1)$$

where $k^v$ denotes the thermal conductivity of the vapor, $\Delta T$ the temperature difference between the solid substrate and the saturation temperature of liquid at the given pressure, $\mu^v$ the viscosity of the vapor, $\rho_l$ the density of liquid, $g$ the gravitational acceleration, $h_{fg}$ the enthalpy of the liquid-vapor phase change, $\rho_v$ the density of vapor phase, and $\gamma$ the surface tension of the liquid-vapor interface. On the other hand, for droplets with a radius larger than the capillary length, the thickness of Leidenfrost film is proportional to $R^{1/2}$. Snoeijer et al.[50] and Sobac et al.[93] developed a more comprehensive and general model to predict the shape of vapor film underneath of a Leidenfrost droplet. Their model predicts the radial dependence of film thickness, which was not considered in the earlier models.

As shown in Figure 1a, the decoupled hierarchical structure includes a superhydrophilic nano membrane, which is joined on top of a deep Si micro-pillar structure. The height of pillars in the deep microstructure should be high enough to reduce the developed pressure by shear flow of the vapor in the microstructure. Through simulation of vapor flow, we found that the pillars with a height of > 95 μm is required to suppress LFP at high temperatures. Once a droplet contacts the nano membrane, the capillary force per unit area by the nano-pores, which is $\Delta \mathrm{P}_{capillary} = 2\gamma \cos\theta / r_p$, keeps the droplet in contact with the nano membrane. Note that $\theta$ and $r_p$ denote the contact angle of liquid meniscus formed in the nano-pores and radius of the nano-pores, respectively. Liquid forms spherical meniscus in the nano-pores as the dimension of nano-pores is much smaller than the capillary length of the liquid. At the liquid-vapor interface, evaporation occurs to dissipate heat flux by the hot solid substrate. The generated vapor flows in the microstructure radially and leaves the structure from the sides. Note that the shear loss for vapor upward flow through nano-pores is proportional to the thickness of the membrane divided by the square of pores' diameter. This shear loss is 2-3 orders of magnitude higher than the shear loss through the microstructure. Thus, the generated vapor flows predominantly radially in the microstructure. If the de-wetting force by vapor flow overcomes the capillary force, the droplet will detach from the substrate and adopt the Leidenfrost state. Note that these forces are decoupled and independent. These forces can be modified independently to tune the LFP. We simulated the vapor flow in the microstructure to obtain an insight on pressure field of vapor. The details of simulation are given in the Supplementary Information. Also, we provide an approximate analytical solution of maximum pressure generated by the vapor flow in the Supplementary Information. In **Figure 5b**, the velocity field of the vapor in the microstructure is shown. Although the vapor velocity reaches high values, the assumption of laminar flow field is still valid. We examined the cooling effect of pillars by the vapor. For the vapor flow in the microstructure, we calculated the Reynolds numbers. The hydraulic diameter of the microstructure is $\mathrm{D}_H = 75\ \mu$□. The calculated Reynolds number is $4 \leq Re \leq 540$. Thus, flow of the vapor in the microstructure is laminar. For this given Reynolds number, the hydrodynamic entry length is $\mathrm{Le}_{\mathrm{Hydrodynamic}}$ = (0.05 $\mathrm{D}_{\mathrm{H}}$ Re), which is 15 $\mu m$-2 mm. Thus, flow in the microstructure is not fully developed. Also, the thermal entry length for the vapor is written as $\mathrm{Le}_{\mathrm{Themal}}$= (0.05 $\mathrm{D}_{\mathrm{H}}$ Re Pr), which is 15 $\mu m$-2 mm as well. Pr denotes Prandtl number. The Nusselt number for the configuration of undeveloped hydrodynamic and thermal boundary layers is calculated by T. Irvine et al.[94] as a function of length of vapor flow. Given these Nusselt numbers and thermal conductivity of steam ($k_{steam}$= 0.018 Wm$^{-1}$k$^{-1}$), we determined the values of heat transfer coefficient as shown in the Table 1. We calculated the Biot number in the structure ($Bi = \frac{h\,w}{2\,k_{Si}}$), where $w$ denotes the width of micro-pillars, and $k_{Si}$ the thermal conductivity of Si, 148 Wm$^{-1}$k$^{-1}$. The maximum Biot number is 0.00014 suggesting that the pillars are isothermal. The cooling heat flux by the vapor flow is written as $q_s = h\,(T_s - T_m)$, where $T_s$ denotes the surface temperature of pillars, and $T_m$ the mean temperature of vapor. In Table 1, we compared the ratio of cooling heat flux to the total heat flux $(q_s/q_{total})$ as a function of radial length underneath of the droplet for different surface temperatures. As shown, as low values of superheat, the convective cooling by the vapor can be up to 20% of the total heat flux, but at high temperatures, this cooling effect becomes negligible. Also, the vapor flow on the nano-membrane can lead to a temperature gradient in the nano-membrane, as the thermal conductivity of this membrane is low. Given the heat transfer coefficient by the vapor phase and its mean temperature, one can determine the cooling heat flux on the membrane at different temperatures. Using Fourier definition of heat flux and length scale of distance between pillars, the change in temperature of nano-membrane induced by vapor cooling effect is 4-9 $^{o}$C, which has a small effect on local evaporation rate.

Through the simulations, we determined the generated pressure field in the microstructure during the vapor flow as shown in **Figure 5c**. If the maximum generated pressure in the microstructure is less than the induced capillary pressure by the nano membrane, the droplet will remain attached to the nano membrane and the Leidenfrost state is suppressed. Through these simulations, we can compare the ratio of pressures by the shear flow of vapor and the capillary of nano pores at different temperatures. This ratio is shown in **Figure 5d** for several dimensions of nano membranes. Note that for all the considered nano membranes, no Leidenfrost state occurs even up to temperature of 700 $^{o}$C.

As the required microstructure should be deep (height of 95 ± 2 μm), we developed a custom-designed micro-fabrication procedure for these structures. The details of this approach are provided in the Experimental Methods. After fabrication of the microstructure, we used a sintering approach to attach the nano membrane to the Si micro pillars. A schematic of this approach is shown in **Figure 6a**. In this approach, one utilizes Au as the interlayer between the membrane and the microstructure[95]. One side of the membrane is coated with Au in the e-beam evaporator with a thickness of 300 nm. Also, the top of the micro pillars is coated with a thin layer of Au having a thickness of 500 nm. To open the nano pores, the nano membrane is physically etched using RIE180. The coated samples are assembled on top of each other and a pressure of 2 MPa was applied to the sample. The sample is sintered at a temperature of 600 $^{o}$C. The picture of the developed microstructure in this work is shown in **Figure 6b**. We used Anodic Aluminum Oxide (AAO) as the nano membrane. These membranes with varied pore diameters were obtained from Synkera Technologies Inc. These membranes have a diameter of 25.4 mm, a thickness of 50 μm and a pore density of 10% reported by the manufacturer. As we needed to develop a structure to be used for high temperatures, the AAO membrane were heat treated by the manufacturer for operating temperature of up to 1000 $^{o}$C. Although as-made AAO membranes are amorphous and have low thermal conductivity, the heat treated AAO membrane by Synkera Technologies Inc. are crystalline α and γ alumina phases and have thermal conductivity of approximately 30 $Wm^{-1}K^{-1}$.[96] We needed the contact angle of water in the nano pores to determine capillary pressure in these pores. To do so, as shown in **Figure 6c**, we measured the contact angle of a water droplet on a pre-cleaned nano membrane and used this contact angle to determine the capillary pressure in the pores. The nano-membrane was cleaned with plasma cleaner (Harrick Plasma PDC-001-HP) before these measurements. The measured contact angle of a water droplet on these nano membranes is 3 ± 1$^{o}$. The final developed structure is shown in **Figure 6d**.

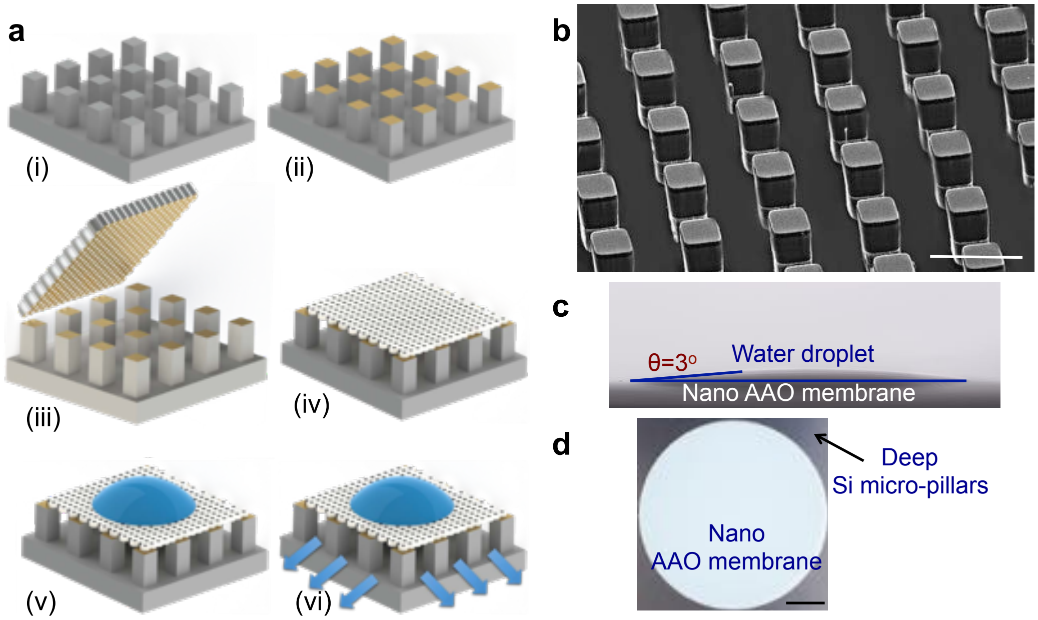

**Figure 6**. a) A schematic of fabrication steps of decoupled hierarchical structure is shown. (i) The deep Si microstructure was fabricated in the first step. (ii) A layer of Au film with thickness of 500 nm was coated on the pillars through e-beam evaporation (Thermionics E-beam evaporator). Also, a thin layer of Au, 300 nm, was coated on the back-side of the nano membrane. The pores in the nano membrane were opened through etching with RIE180 from the front side after Au deposition. (iii) The nano membrane and the microstructure were assembled on top of each other. (iv) The structure was sintered at pressure of 2 MPa and temperature of 600 °C for 3 hrs. (v) A sessile droplet was deposited on the surface. (vi) The nano membrane keeps the droplet attached to the structure, while the microstructure provides a path for vapor flow. b) The structured of deep Si micro-pillar structures is shown. These micro pillars are developed through a custom-designed fabrication process. The height of pillars is 95 ± 2 μm. The microstructure is tilted 45° in the SEM sample holder to capture this picture. The scale bar is 100 μm. c) The contact angle of a water droplet on the AAO nano membrane is measured. The membrane shows superhydrophilic characteristics. d) The developed decoupled hierarchical structure is shown. The deep Si micro-pillar structure provides a path for vapor flow, while the nano membrane keeps the cooling droplet attached to the substrate through the capillary force. The scale bar is 5 mm.

The penetration of liquid through the nano-membrane to the microstructure is a time-dependent process. Once a droplet is deposited on the nano-membrane, the wicking rate is governed by the balance between the capillary force and the shear force of the fluid in the nano-pores (i.e. Washburn's law[97]). The time scale for liquid wicking is written as

$$\tau_{wicking} \sim \frac{2\,\mu\, t^{2}}{\gamma\, r \cos\theta} \qquad (2)$$

where $\mu$ denotes the dynamic viscosity of liquid, t the thickness of nano-membrane, $\gamma$ the surface tension of liquid, $r$ the radius of nano-pores and $\theta$ contact angle. In the decoupled hierarchical structures, the thickness of nano-membrane is 50 $\mu$m. For the pore radius of 40 nm, the penetration time is in order of $10^{-3}$ s. At room temperature, a nano membrane was placed on a smooth Si wafer. After deposition of a liquid droplet, it takes several seconds before wetting of the underneath substrate occurs. At high temperatures, while liquid wicks in the nano-pores, it also evaporates. The time scale for evaporation of liquid in a pore is written as

$$\tau_{evap} \sim \frac{t\,\rho\,h_{fg}}{\dot{q}}$$

where $\rho$ denotes density of liquid, $h_{fg}$ the enthalpy of phase-change and $\dot{q}$ the heat flux. The heat fluxes in the experiments are in order of $10^5$-$10^7$ $\mathrm{Wm^{-2}}$. Thus, $\tau_{evap}$ is in order of $10^{-3}$-$10^{-5}$ s. The time scale for evaporation is smaller than wicking time and consequently the liquid cannot wick to the microstructure and vapor phase occupies the microstructure domain.

Once the decoupled hierarchical structure was developed, we examined the heat dissipation by these new structures. Each structure was thoroughly cleaned by plasma cleaning and was placed on the heating stage. Through fluid dispensing systems, droplets of DI water with a volume of 30 $\mu L$ were introduced on the structure at a height of 4 mm (We~4.4). We minimized the distance between the droplet and the structure to suppress the role of droplet inertia on the droplet spreading. The temperature of the structure was measured close to the droplet deposition coordinate with two independent thermocouples. These thermocouples are attached to the structure with a thermal paste (OMEGA THERM 201). We measured the phase change characteristics of the water droplets as a function of temperature on these surfaces. These characteristics are captured using a high-speed camera (V711, Vision Research). The phase change characteristics on decoupled hierarchical structures are shown in **Figure 7**. As shown, at low value of superheat, the droplet is attached to the surface through the capillary force and thin film evaporation occurs underneath of the droplet. As the porosity of the studied membrane is only 10%, the evaporation rate of the droplet is small. As we increase the temperature, the phase-change characteristic enters a new regime in which nucleate boiling and thin-film evaporation occur simultaneously. Thus, the evaporation time of the droplet is reduced. We have shown the phase-change characteristics of a water droplet for four temperatures. Note that even up to a temperature of 540 $^{o}$C, we did not observe the Leidenfrost state. Note that the maximum measured Leidenfrost temperature on state-of-the-art surfaces is 453 $^{o}$C[74]. The common approach to determine LFP and heat dissipation characteristics of a surface is measurement of the evaporation time as a function of temperature[98]. In **Figure 7a**, we plotted water droplet evaporation time as a function of temperature on the decoupled hierarchical structures. We developed these decoupled hierarchical structures with two nano membrane pore dimensions and examined their phase-change characteristics as shown in **Figure 7b**. As the porosity of the nano membranes are the same, the difference in the evaporation rate cannot be related to the enhanced surface area for evaporation. We expect that the observed difference in the evaporation rate is caused by the non-uniform distribution of pores on the surface. As the characteristic curve shows, through decoupling of the de-wetting force of vapor flow and the capillary force, Leidenfrost state is suppressed. However, the evaporation time of the droplets on these surfaces is higher than the state-of-the-art surfaces. This high evaporation time is caused by two effects: low thickness of nano membrane and inadequate active site for heterogeneous nucleation of vapor bubbles on the smooth nano membrane surface. Phase-change process occurs through nucleate boiling on the flat surface of nano membrane and evaporation in the nano pores.

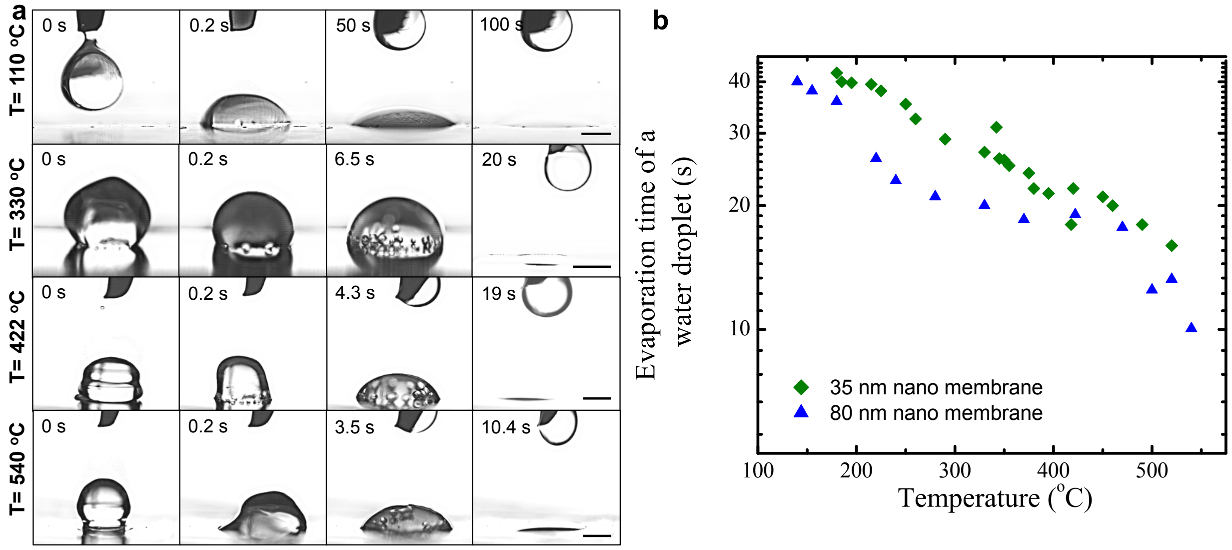

**Figure 7.** a) The phase-change characteristics of a water droplet on smooth decoupled hierarchical structure are shown. The pore dimension in this nano membrane is 80 nm. At low value of superheat, only thin film evaporation at the nano pores dissipates heat. However, at high superheats, some nucleate boiling enhances the heat dissipation by the structure. Note that no LFP was observed even to temperature of 540 °C. b) The droplet evaporation time by two types of decoupled hierarchical structure is measured. The evaporation time is a decreasing function of temperature.

Heat for phase-change process is transferred through Si pillars and then laterally in the nano membrane between pillars. Low thickness of nano membrane reduces the heat capacity of the structure and consequently the total heat flux for phase-change in the decoupled hierarchical structures.

Before contact of the droplet with the de-coupled hierarchical structure, the thermal resistance through convection and radiation is much higher than the conduction thermal resistance in the hierarchical structure. Thus, the structure is approximately at a uniform temperature. The reported temperature is the temperature on the membrane surface. However, the surface temperature underneath of the droplet will drop as the droplet touches the surface. We emphasize that the temperature of droplet cannot exceed the spinodal decomposition temperature of water at ambient pressure[99–101] (321 ± 17 °C).

To overcome the shortcoming of high evaporation time on these smooth decoupled structures, we enhanced the nucleation sites of bubbles on the nano membranes through deposition of NPs. We deposited a layer of $SiO_2$ NPs on the decoupled hierarchical structure with nano pore dimension of 80 nm. The detail of the deposition approach is given in the Experimental Methods. Once the coated decoupled hierarchical structure is developed, we examined heat transfer characteristics of this structure on the heating stage. These characteristics are shown in **Figure 8a**. Similar to the previous structures, we observed two regimes of phase-change. At low values of superheat, thin film evaporation at the mouth of the nano pores occurs and the phase-change characteristics are similar to the decoupled hierarchical structures without coated NPs. However, as we increase temperature, the nucleation sites on the surface are activated and we observe the transition to the thin-film evaporation/boiling regime. The phase-change on these structures is more chaotic as enhanced boiling on the nano membrane surface occurs. We continued these experiments to a temperature of 570 °C. No LFP was observed on these decoupled hierarchical structures. The characteristics curve of evaporation time of a water droplet on these surfaces is shown in **Figure 8b**. As shown, at high values of superheat the evaporation time on these surfaces is reduced by approximately two orders of magnitude. Nucleate boiling at the nano membrane surface and evaporation at the mouth of nano pores are responsible for this remarkable evaporation rate. Note that the developed structures are sintered at 600 °C, and conducting experiments at higher temperatures (> 570 °C) affects the integrity of the structure. However, once higher temperature joining approach is implemented, these structures can be operated at higher temperatures.

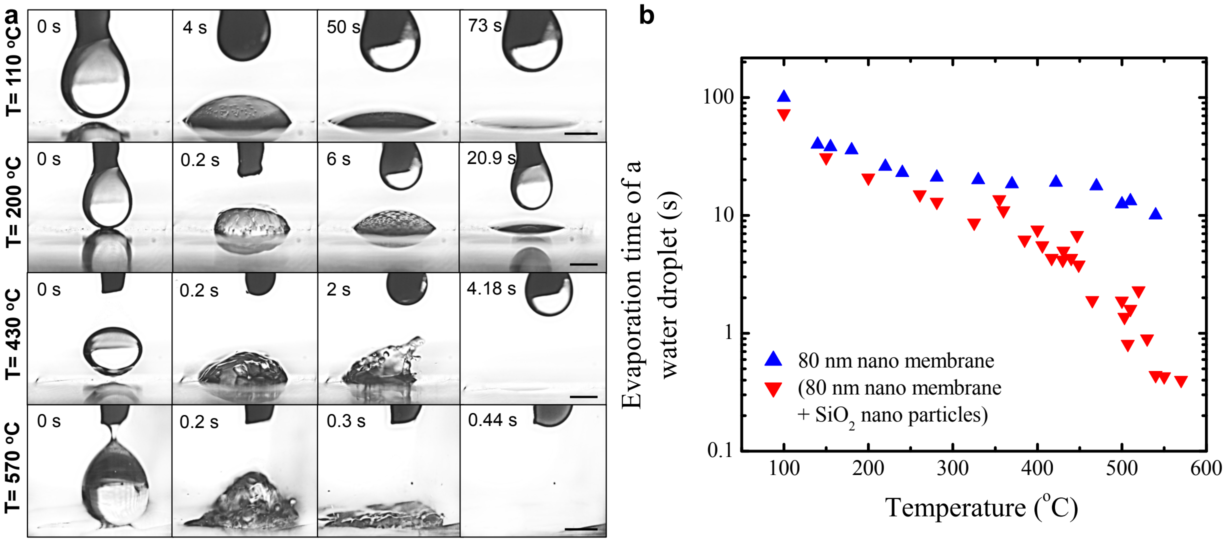

**Figure 8.** a) The phase-change characteristics of a water droplet on NP coated decoupled hierarchical structure at four temperatures are shown. At low values of superheat, the heat is dissipated through thin film evaporation. At higher values of superheat both thin-film evaporation at the mouth of nano pores and nucleate boiling occurs. No LFP was observed on these decoupled hierarchical structures even up to 570 °C. The scale bar in the figures is 2 mm. b) The evaporation time of a water droplet on the decoupled hierarchical structure and NP coated one are compared. As noted, at high temperatures, the evaporation rate and consequently the heat dissipation by the NP coated decoupled hierarchical structure is two orders of magnitude higher than the other surface.

We compared heat transfer characteristics of the NPs coated decoupled hierarchical structure with other state-of-the-art surfaces as shown in **Figure 9a**. One of the structures is a hierarchical structure[74] in which Si micro-pillar structure is coated with $SiO_2$ NPs through layer-by-layer deposition. The procedure for this deposition was initially proposed by Iler[102] and further improved for aqueous solutions by Lee et al.[103] The onset of film boiling in this structure is at a temperature of 250 °C, and the LFP occurs at a temperature of 453 °C. The other state-of-the art structure is a zirconium nanotube structure[92], which is developed through anodic oxidation technique with hydrofluoric acid (0.5%). The onset of film boiling on this structure is close to 250 °C and LFP occurs at a temperature of 350 °C. LFP of around 400 °C is also reported by kwon et al.[66] in Si hierarchical structures, but the characteristic curve of evaporation time was not reported. The Leidenfrost temperature on the decoupled hierarchical structures is suppressed up to temperature of 570 °C. Note that at low value of superheat, the existence of vapor layer adversely affects the heat dissipation capacity of decoupled hierarchical structures. However, at high value of superheat these surfaces outperform other state-of-the-art structures in heat dissipation. Furthermore, the heat flux by decoupled hierarchical structure and other state-of-the-art structure are shown in **Figure 9b**. The heat flux is determined through evaporation time and contact area of the droplet with the surface. As shown, the developed decoupled hierarchical structure in this work shows a distinct characteristic compared to the other structures. We should add that Vakarelski et al.[67] used superhydrophobic structures to stabilize the film-boiling region on a hot object leading to low heat dissipation capacity. However, through decoupled hierarchical structures, one can keep high heat dissipation capacity at high temperatures through nucleate boiling and thin-film evaporation.

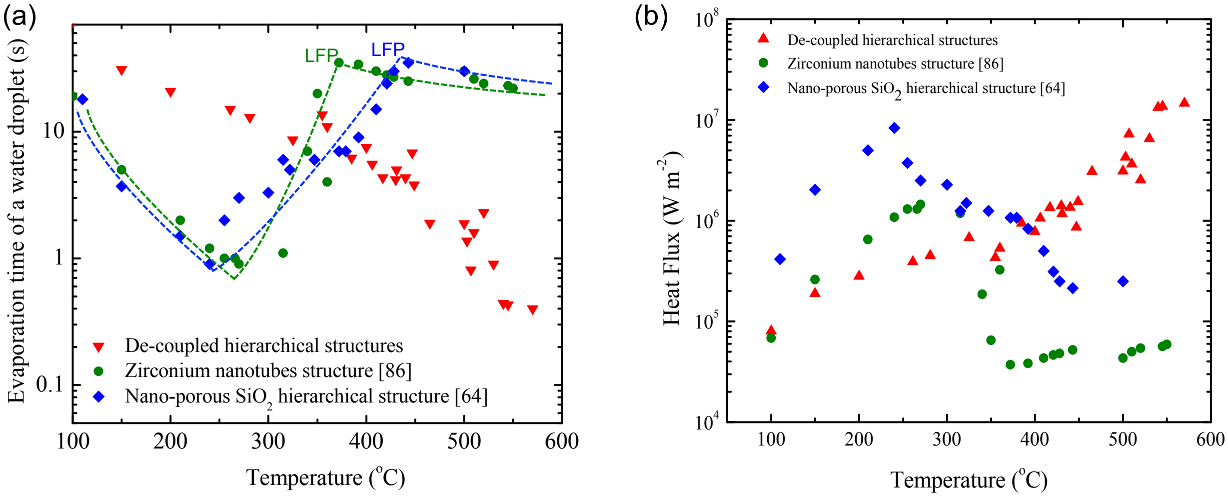

**Figure 9.** (a) The phase-change characteristic on decoupled hierarchical structures is compared with state-of-the-art surfaces. On the other surfaces, Leidenfrost state occurs and limits heat dissipation capacity by these surfaces. The independent tuning of capillary pressure and the de-wetting pressure of vapor allows suppression of LFP in decoupled hierarchical structures. These new surfaces offer two orders of magnitude higher heat dissipation capacity compared to the other surfaces at high temperature. (b) Heat flux by the decoupled hierarchical structure is compared with other state-of-the-art surfaces. The heat flux is determined through the evaporation time of the droplet and the contact area at different temperatures.

For water droplets, no LFP was observed on Si decoupled hierarchical surfaces even up to a temperature of 570 °C. In these structures, the capillary force for contact of a droplet to a hot surface and de-wetting force by the vapor phase are independently tuned to suppress LFP. These structures showed up to two orders of magnitude higher heat flux at high temperatures, but at low values of superheat, the heat dissipation capacity was inferior to other surfaces. Here, based on the same concept, we report a new metallic surface that shows no LFP and offers high heat dissipation capacity at all superheat ranges. These surfaces are developed through one-step fabrication procedure with no required micro/nano fabrication and promise a new and cost-effective route for high heat dissipation capacity. In Si decoupled hierarchical structures, a nano-membrane keeps the droplet in contact with the surface through a capillary force, while high-aspect ratio micro-pillars provides a path for vapor flow. The capillary force, $F_c$, is a function of radius of nano-pores and the de-wetting force, $F_v$, by vapor is a function of dimension of micro-pillars. As these forces are independent, tuning of these forces allows to satisfy LFP suppression criterion (i.e. $F_c/F_v > 1$).

The schematic of Cu decoupled hierarchical structures is shown in **Figure 10**. In these structures, a stack of corrugated Cu meshes are used to provide a path for vapor flow (similar to micro-pillars) and multi-layers of Cu micro/nano particles are exploited to form a nano-porous surface (similar to nano-membrane) to impose capillary forces on the liquid.

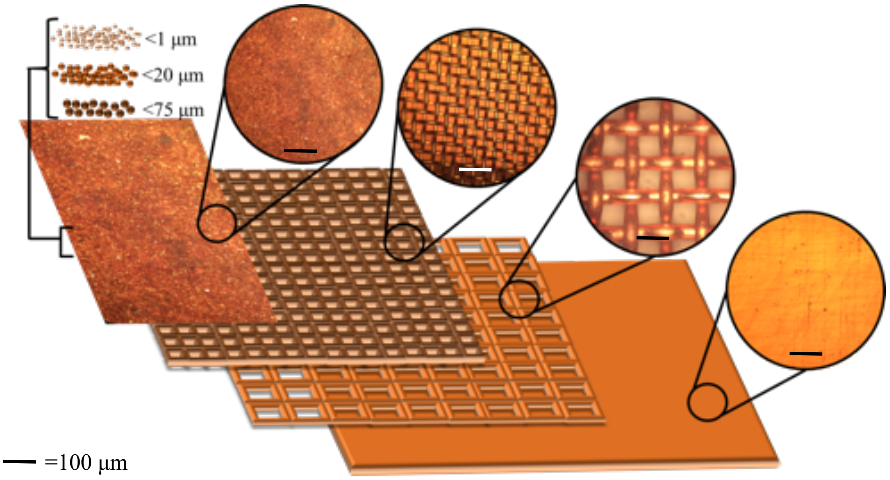

**Figure 10:** A schematic of Cu decoupled hierarchical structure is shown. The structure is composed of a stack of two corrugated Cu meshes and multi-layers of micro and nano Cu particles. The Cu meshes provide a path for radial vapor flow, while the nanoparticles provide a nano-porous surface for capillary force to keep the cooling droplet in contact with the hot surface.

The development procedure of Cu decoupled hierarchical structures is shown in **Figure 11**. On a flat and smooth Cu substrate, corrugated Cu meshes (TWP Inc.) with two dimensions of 200 μm and 75 μm are vertically stacked. This dimension represents the opening dimension in meshes. Cu spherical particles with diameter of <425 μm (Sigma Aldrich), <75 μm (Sigma Aldrich), and 60-80 nm (SkySpring Nanomaterials) are obtained. To deposit Cu particles, each size of particles are mixed with isopropanol alcohol to form three homogenous dilute suspensions (30 wt\%). Initially, a layer of Cu particles with dimension of <425 μm was deposited on the stack of Cu meshes through a dip coating process in the suspension. We continued the dip coating process for three times to form a uniform layer of Cu particles. Next, Cu micro particles with dimension of < 75 μm were deposited through dip coating method. Finally, the surface is furnished with Cu nanoparticles (60-80 nm). Once the nanoparticles are coated on the surface, the Cu decoupled hierarchical structure was placed in the furnace with inert flow gas environment (Nitrogen). This gas environment was required to prevent oxidation of Cu in the sintering process. The structure was sintered at temperature of 1050 $^{o}$C for 1 hr. The heating and cooling rate in the furnace was 6 $^{o}$C per min. The final Cu decoupled hierarchical structure is shown in **Figure 11(i)**.

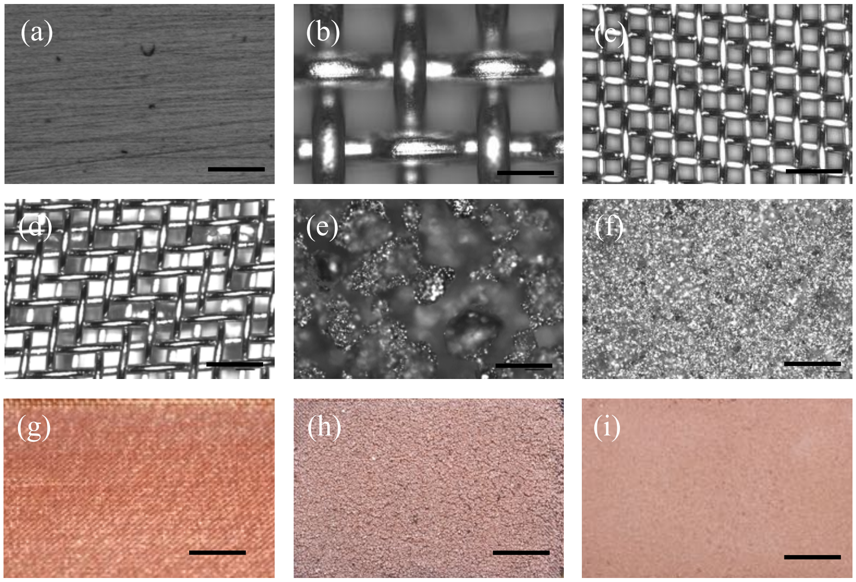

**Figure 11:** The development procedure of Cu decoupled hierarchical structure is shown. (a)-(c) Two Cu meshes are assembled on a flat Cu substrate. (d)-(f) three layers of micro/nano particles are deposited on the stack of Cu mesh through dip coating approach. The scale bar in subfigures (a)-(f) is 200 μm. (g) The stack of Cu meshes, (h) the surface after the coating of micro/nano particles, and (i) the final Cu decoupled hierarchical structure after sintering is shown. The thickness of the final structure is 1 mm. The scale bar in subfigure (g)-(i) is 1 mm.

The capillary force and de-wetting force by the vapor phase per unit area may be written as

$$F_v \approx \frac{\mu_v \dot{q} L}{\rho_v h_{fg} d^2}$$

$$F_c \approx \frac{2\gamma_{lv} \cos\theta \, \zeta}{r}$$

where $\mu_v$ denotes dynamic viscosity of vapor phase, q heat flux, L length of vapor flow, $\rho_v$ density of vapor phase, $h_{fg}$ enthalpy of liquid-vapor phase-change, d characteristic diameter for vapor flow in corrugated mesh, $\gamma_{LV}$ surface tension of liquid-vapor, θ contact angle of liquid and the surface, and ζ density of nano-pores on the surface. As the experiments had to be conducted at ambient condition, Cu structure could oxidize at high temperature > 200 °C). Thus, we decided to examine these surfaces with non-aqueous liquids with lower boiling point. We chose Novec 7100 liquid (3M Co.) for these experiments. This liquid is highly wetting liquid of Cu, has boiling temperature of 75 °C, surface tension of 13.6 $Nm^{-1}$, liquid density of 1510 $kgm^{-3}$, liquid dynamic viscosity of 0.58 mPa.s and enthalpy of evaporation of 112 kJ $kg^{-1}$. At maximum heat flux of $10^7$ $Wm^{-2}$, for the corrugated mesh with the average opening of 200 μm, 1 m length of vapor flow, a nano-porous surface with pore density of 0.5, and pore radius of 80 nm, the ratio of $F_c/F_v$ is approximately 4. This suggests that even for extreme heat fluxes, the LFP could be suppressed on Cu decoupled hierarchical structures.

To examine heat transfer characteristics of Cu decoupled hierarchical structures, we studied phase-change characteristics of Novec 7100 liquid droplets on these surfaces. Initially, we studied the phase-change characteristics on a smooth Si wafer and micro-structured Si substate. The Si microstructure is a micro-pillar structure with dimension of 95 μm in height, 40 μm in pillar width and 60 μm in pillar spacing and is developed through micro-fabrication procedure. This high aspect ratio pillars allow for low shear resistance for vapor flow. A Novec 7100 droplet with volume of 30 μL was deposited on the substrate at various temperatures and phase-change characteristics was recorded with a high speed camera (Phantom V711, vision research). These characteristics at various temperatures are shown in **Figure 12**. At low superheat values, the droplet goes through nucleate boiling process. However, at high superheat values, Leidenfrost state emerges and the heat transfer rate becomes minimal. (i.e. heat transfer occurs through conduction in a thin vapor film underneath of the droplet). This slow heat transfer rate boots the droplet evaporation time. The LFP for both Si and Si micro-structured surfaces are around 45 K superheat. Next, we examined phase-change characteristics of Novec 7100 droplets on a flat Cu substrate and Cu decoupled hierarchical structures as shown in **Figure 13**. For Cu substrate, the similar transition to LFP at high superheat values occurs. However, for Cu decoupled hierarchical structures, no LFP state was observed even at superheat value of 125 $^{o}$C. As we conducted the experiments in ambient condition, we did not continue the experiment at higher temperatures than 220 $^{o}$C to avoid Cu oxidation. In the Cu decoupled hierarchical structure LFP is suppressed and high heat dissipation capacity is achieved through nucleate boiling at all temperature ranges.

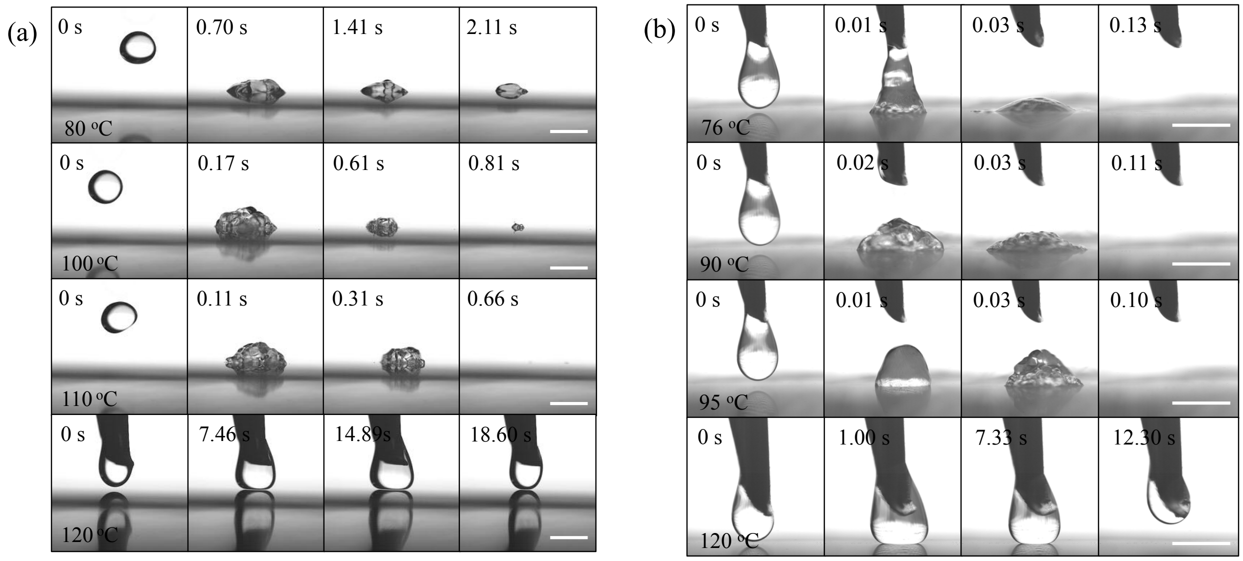

**Figure 12:** Phase-change characteristics of a Novec 7100 droplet on (a) smooth Si wafer and (b) micro-structured Si is shown. At low superheat values, the liquid droplet goes through nucleate boiling, but at high superheat values, the droplet adopts a Leidenfrost state. Note that at temperatures higher than LFP, the liquid droplet rolls on the surface. Thus, the dispensing needle is used to keep the droplet stationary for imaging purpose. The scale bar is 2 mm.

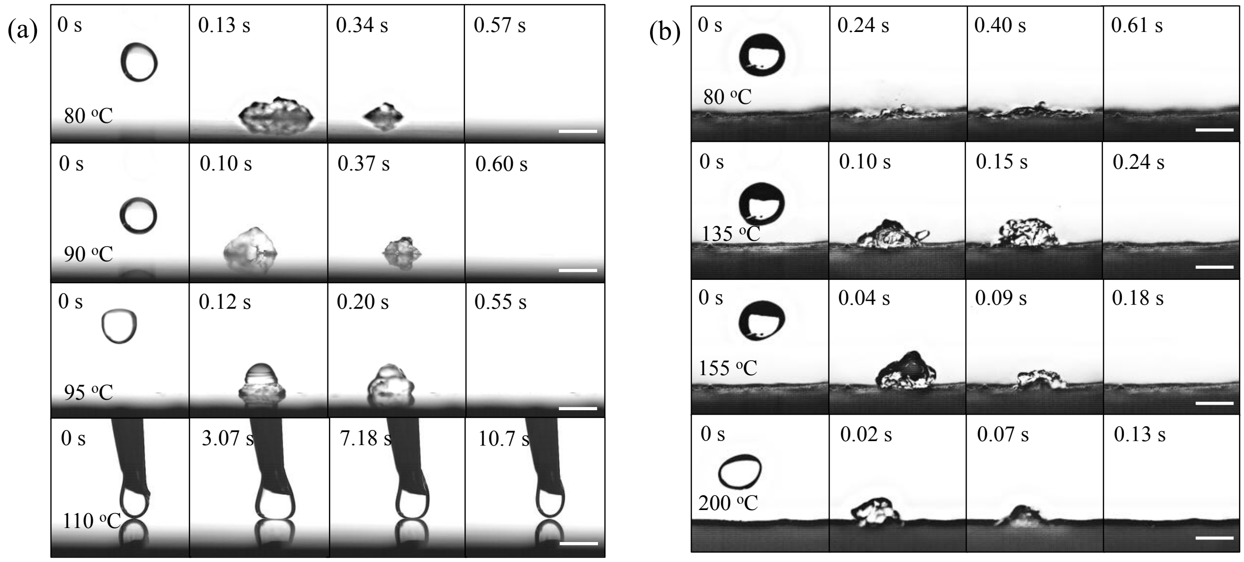

**Figure 13:** Phase-change characteristics of a Novec 7100 droplet on (a) smooth Cu substrate and (b) Cu decoupled hierarchical structures is shown. Although for Cu substrates, Leidenfrost state emerges at high superheats, no LFP was observed on decoupled hierarchical structures. The scale bar is 2 mm.

To acquire an understanding of heat dissipation capacity of various substrates, we plotted droplet evaporation time as a function of temperature in **Figure 14a**. We also conducted similar experiments on Si decoupled hierarchical structures. As shown at low values of superheat, for Si, micro-structured Si, and Cu, the evaporation time is a decreasing function of temperature and reaches a minimum corresponding to maximum heat flux. After, there is a transition regime in which the droplet evaporation time increases as a function of temperature reaching to LFP in which the heat transfer rate is minimal. For decoupled hierarchical structures, there is no LFP as also shown in the images of phase-change in Figure 13. However, for Cu decoupled hierarchical structures, we observed an interesting trend. No LFP implies that the droplet evaporation time should monotonically decreases with time, which is consistent when the wall super heat value is more than 15 $^{o}$C. However, at low superheat values, we observed an inverse trend in which droplet evaporation time increases with temperature. We also noted that at low value of superheat, micro-structured Si has higher heat dissipation capacity than Cu decoupled hierarchical structure. The higher exposed surface area of Si micro-structured surface for phase-change could explain the higher heat dissipation capacity. However, the opposite trend at low superheat values is a matter of question.

To understand this reverse trend, we probed the transient temperature of the Cu decoupled hierarchical structure underneath of the droplet. A k-type thermocouple with diameter of 250 μm was placed at the surface of the Cu decoupled hierarchical structure where the liquid droplet lands. The transient temperature profile of the surface underneath of the droplet is shown in **Figure 14b**. The time scale starts at 1 sec before the contact of the droplet on the surface. As shown, before the contact, the surface is isothermal. However, once the droplet touches the surface, a local cooling occurs underneath of the droplet and the temperature of the surface may fall below the phase-change temperature (75 $^{o}$C). In this case, the droplet does not experience phase-change at the surface and wicks through the structure due to high capillary forces. The time scale for droplet penetration is determined by balance of the capillary force and viscous shear force of the liquid in the structure and is written as

$$\tau_{wicking} \approx \frac{2\mu_l t^2}{\gamma_{lv} r \cos\theta}$$

where $\mu_l$ denotes viscosity of liquid, t thickness of the Cu decoupled hierarchical structure, and r characteristic pore dimension in the structure. For the thickness of 1 mm and characteristics pore dimension of 1 μm, the wicking time scale is approximately 85 ms. This time scale is several times smaller than the phase-change time shown in **Figure 13b** at low superheat values. That is, the droplet does not wick completely through the structure. While the fluid is wicking in the structure, it contacts higher temperatures regions and goes through a phase-change process in the structure. This is schematically shown in the subset of Figure 14. Since the phase-change process occurs inside the structure, the images do not show the actual phase-change time. That is, the phase-change time is higher than what is shown in **Figure 13**. However, as temperature increases, the wicking length of the droplet will reduce, and the images provide exact time of the droplet evaporation. Thus, local cooling underneath of the droplet clarifies the inverse trend observed in **Figure 14a**.

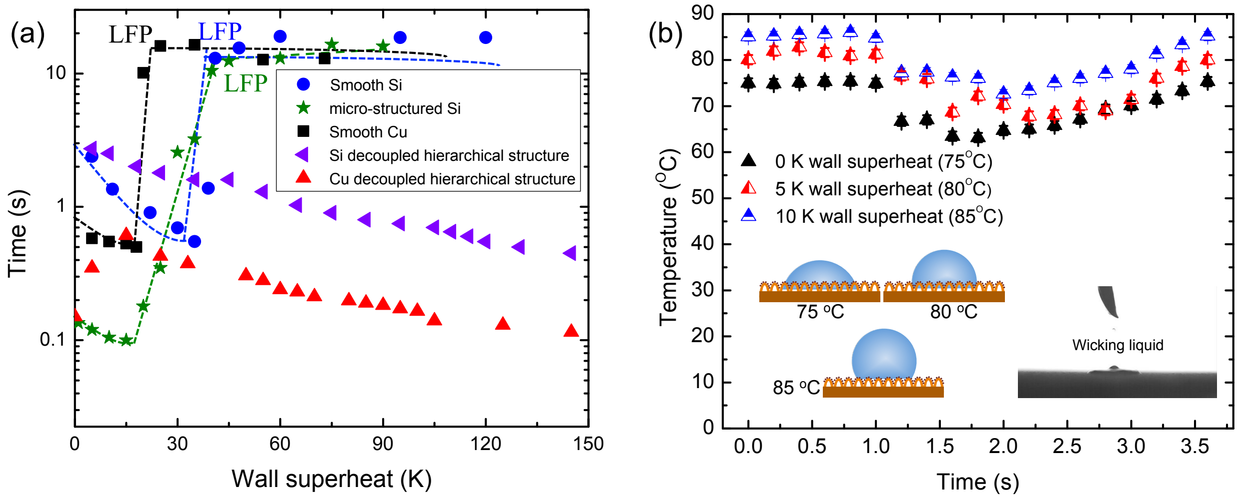

**Figure 14**: (a) The evaporation time of a Novec 7100 droplet with volume of 30 μm on various solid surfaces are compared. In contracts to all the other surfaces, Cu decoupled hierarchical structure does not show any LFP and provides high heat dissipation capacity at all temperature ranges (b) The local temperature of Cu decoupled hierarchical structure is shown before and after contact of the liquid droplet. The liquid droplet touches the surface at 1 sec. The local subcooling of the surface drops the local temperature below the phase-change temperature. Consequently, the liquid partially wicks in the structure before experiencing the phase-change.

We plotted the heat flux as a function of temperature for all the studied surfaces in **Figure 15**. The heat flux is determined based on the droplet evaporation time and the contact area of the droplet on the surface. We omitted the data points of Cu decoupled hierarchical in which local subcooling and partial wicking in the structure occurred. As shown, Cu decoupled hierarchical structure shows a monotonic trend in heat flux as a function of temperature with no LFP. The heat transfer coefficient on this structure is approximately 20 $kWm^{-2}K^{-1}$ at all temperature ranges.

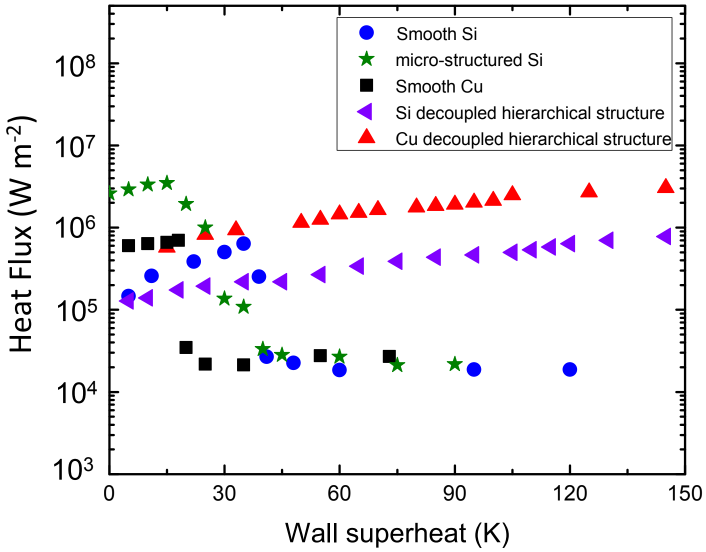

**Figure 15:** Heat fluxes for various solid substrates are shown as a function of temperature. Cu decoupled hierarchical structure shows a monotonic increase in heat dissipation capacity as a function of temperature. The heat transfer coefficient on Cu decoupled hierarchical structure is approximately 20 $kWm^{-2}K^{-1}$ for all temperature ranges.

In conclusion, we present a new surface architecture that suppresses Leidenfrost state and offers high heat dissipation capacity independent of temperature. These surfaces are developed in one-step fabrication with no required micro-nano structuring. Experimental studies on phase-change characteristics of these surfaces show nucleate boiling at all temperature ranges. At low superheat values, once the droplet touches the surface, local surface subcooling occurs that drops the surface temperature below the phase-change temperature. Thus, the liquid partially wicks in the structure before the phase-change. We envision that Cu decoupled hierarchical structures open a new path for high heat dissipation in power generation systems, photonics/electronics, chemical reactors and aviation systems.

## Task 2: Theoretical Study of Nano-Scale Evaporation

In this task, we studied kinetics of evaporation kinetics at small-scale. Although the evaporation in macro-scale has been studied extensively, limitation in the experimental approaches in the nanoscale has precluded sound understanding of the small-scale evaporation. Currently, there are three main theories on the evaporation phenomenon namely Hertz-Knudsen Theory (i.e. Kinetic theory of gases (KTG))[1–3], Statistical rate theory (SRT)[4–7], and Non-equilibrium thermodynamics (NET)[8–10]. The first theory is derived through the kinetic theory of gases (KTG). In budget period2, we demonstrated deficiencies of KTG and SRT approaches and we focused on the NET. The third theory is derived from the non-equilibrium thermodynamics (NET)[8–11]. In this theory, the continuity and momentum equations are integrated over a control volume at the interface. The final form of the evaporation flux without neglecting the cross-effect Onsager coefficients is written as

$$\dot{m} = -C_{mm}\frac{R\,T^L}{M}\ln\left[\frac{P^V}{P^s\,(T^L)}\right] - C_{mq}\,\frac{T^V - T^L}{T^L}$$
$$\dot{q} = -C_{qm}\frac{R\,T^L}{M}\ln\left[\frac{P^V}{P^s\,(T^L)}\right] - C_{qq}\,\frac{T^V - T^L}{T^L} \quad (1)$$

The Onsager reciprocal principal suggests that the cross-effect coefficients must be equal and therefore the coefficient matrix is symmetric. The cross-effect coefficient, $C_{qm}$, couples the heat and mass evaporation fluxes.

In the first budget period, we developed a platform to conduct these small-scale experimental studies as shown in **Fig. 16**. Here, through the custom-made evaporation chamber, we studied the evaporation kinetics at the liquid-vapor interface. The developed experimental setup allows us to acquire accurate knowledge on the interfacial mass and heat transfer during evaporation phenomenon and establish an evaporation theory based on non-equilibrium thermodynamics.

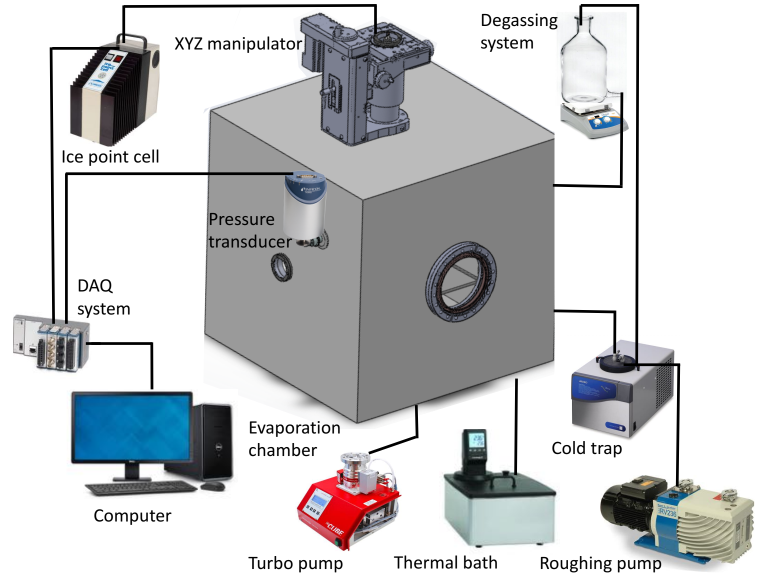

**Figure 16**: The developed chamber for phase-change studies. The chamber is equipped with 2 visible view port, 2 IR transparent view port and embedded feed-troughs, High speed visible and IR camera, Automatic temperature probing system equipped with reference ice point cell, pressure control system, source meter to actuate heat flux, fluid dispensing and accurate flow metering system, cold trap and vacuum system.

All the experiments were carried out in the container with a thermal conductivity of 0.2 Wm$^{-1}$K$^{-1}$, an inner diameter of 44.52 ± 0.01 mm, an outer diameter of 46.35 ± 0.01 mm, and a height of 49.48 ± 0.01 mm, **Fig. 17**. This rounded Polypropylene container with low thermal conductivity, small wall thickness and large diameter leads to small 2D heat losses from the container periphery. To study a wide range of evaporation mass fluxes, the container was mounted on an adjustable heating stage to increase heat flux to the liquid-vapor interface. Temperature of the heating stage was controlled by a thermal bath (VWR, 89202-958) which circulates Ethylene Glycol through the heating stage.

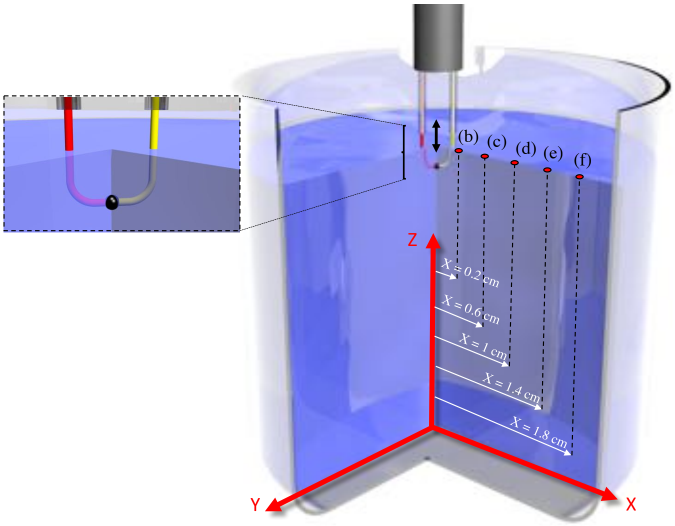

**Figure 17.** A Polypropylene container with an inner diameter of 44.52 mm and an outer diameter of 46.35 mm to hold the liquid. Automated thermocouple with a bead size of ~ 50 µm. Thermocouple wires were passed through two glass tubes with an inner diameter of 0.8 mm. Red dots show horizontal coordinates with their radial distance from the centerline.

For several representative experiments, the thermal field in these two sets of measurement are shown in **Fig. 18**. As shown the thermal field does not change in two hours suggesting steady-state evaporation condition.

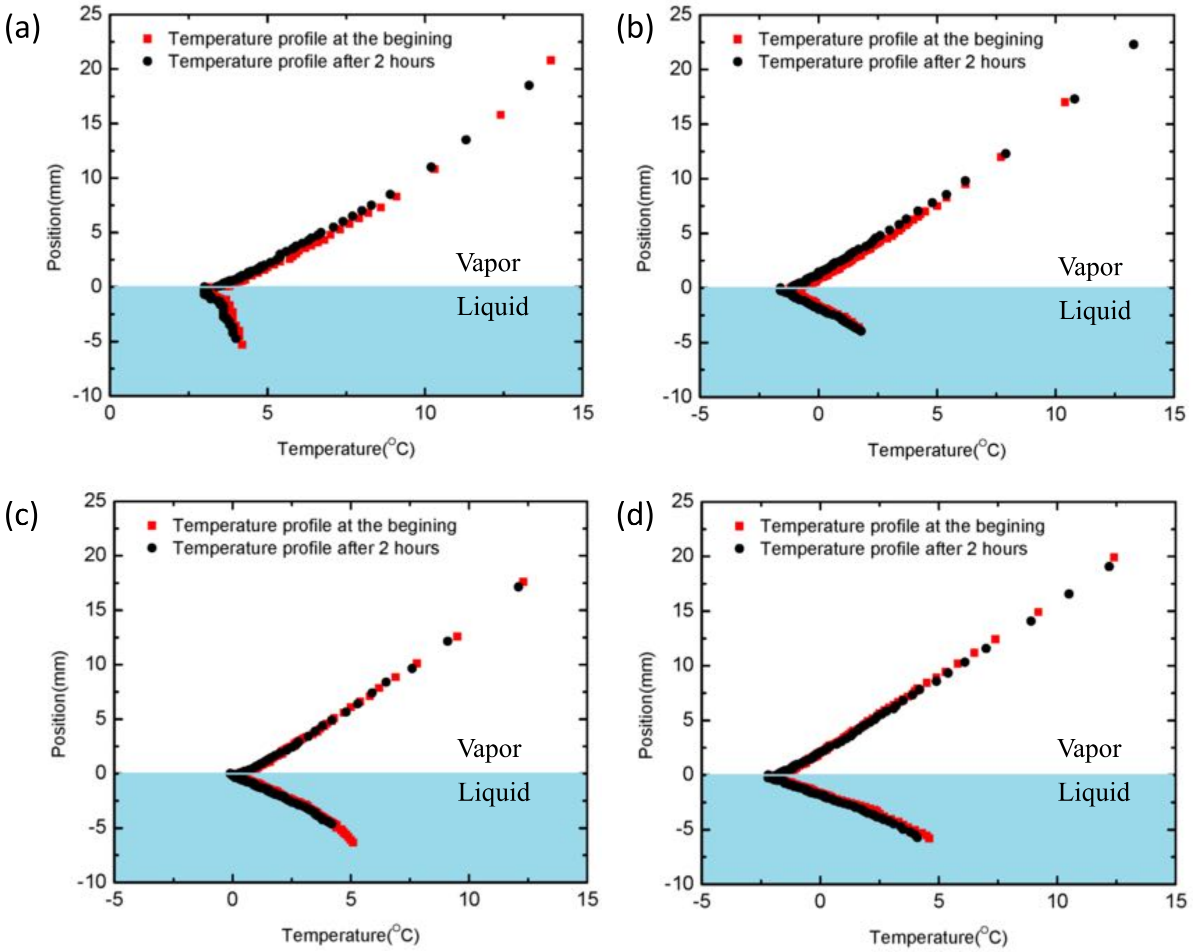

**Figure 18.** Temperature profile at the centerline at the beginning of the experiment and 2 hours after. The thermal field in both phases does not change with time. (a) Vapor pressure in the system was 755 Pa and the heating stage was at the chamber temperature (i.e. 25.4 °C) **,** (b) Vapor pressure in the system was 541 Pa and the heating stage was at 40 °C, (c) Vapor pressure in the system was 613 Pa and the heating stage was at 55 °C, (d) Vapor pressure in the system was 526 Pa and the heating stage was at 70 °C.

Series of steady-state evaporation experiments were conducted on water under different pressure and temperature conditions. In the first set of experiments, the heating stage was at the chamber temperature with no circulating fluid. To study higher evaporative mass fluxes, three more set of experiments were conducted by varying heating stage temperature. The temperature of the heating stage was kept at 40 °C, 55°C, and 70°C in these experiments. In all sets of experiments, the vapor pressure of the system was varied to study the influence of vapor pressure on evaporation. The temperature profiles in the liquid and vapor phases in all these experiments are shown in **Fig. 19**. Note that all these temperature measurements are conducted at the centerline.

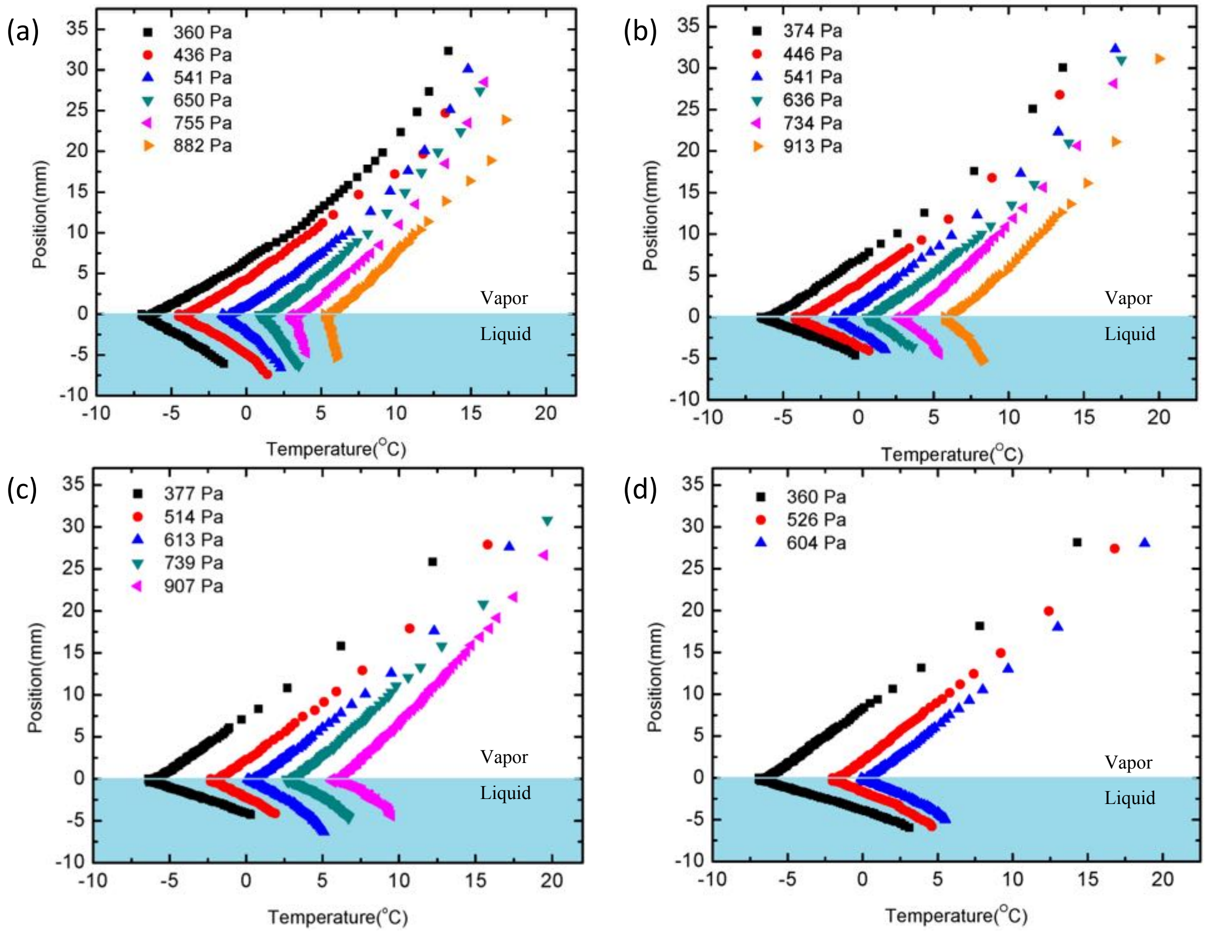

**Figure 19.** Temperature profile at the centerline along the vertical axis for varying heater temperature and vapor pressure in the system. The thermocouple was moved in 50 µm steps close to the interface and the step size was increased further away from the interface. (a) Temperature profile without heater, (b) Temperature profile with the heater at 40 °C, (c) Temperature profile with the heater at 55 °C, (d) Temperature profile with the heater at 70 °C.

In all the experiments, a temperature discontinuity (i.e. temperature jump) of ~ 0.4 °C was evident at the liquid-vapor interface in the direction reported by other literatures[12,13,10,14-15] and the temperature in the vapor phase was slightly higher than in the liquid phase. As shown the minimum temperature occurred at the liquid-vapor interface for all the pressures due to the evaporative cooling effects. The temperature profiles are linear near to the interface, which indicates that thermal conduction is the major mode of energy transport to the interface. The liquid and vapor side heat fluxes were computed from the temperature profiles and listed in **Table 1**. Although the vapor side heat flux was approximately constant, the liquid side heat flux increased by decreasing the vapor pressure. During the evaporation process, a camera with a resolution of 30.25 µm/Pixel was firmly located at the chamber's viewport. Images of the liquid-vapor interface were recorded every 5 mins. Temporal height of the interface was determined through image processing (public domain ImageJ software) and *average* mass flux was determined in each experiment. With the given accuracy of the camera, the corresponding error in the measured total evaporated mass was 0.1-0.3%. However, the mass flux may vary along the interface as shown in other studies[16–19]. If one neglect convection at the interface, by integrating the enthalpy equation over a one-dimensional control volume, the energy equation is written as[20]

$$\dot{q}_l - \dot{q}_v - \dot{m}h_{lv} + \frac{1}{2}\dot{m}^3\left(\frac{1}{\rho_l{}^2} - \frac{1}{\rho_v{}^2}\right) = 0 \tag{2}$$

Where $\dot{q}_l$ and $\dot{q}_v$ denote heat fluxes in the liquid and vapor phases, respectively, $\dot{m}$ is the evaporation mass flux, $h_{lv}$ is the enthalpy of evaporation, $\rho_l$ and $\rho_v$ are densities in the liquid and vapor phases, respectively. The term $(\dot{q}_l - \dot{q}_v)$ is the supplied thermal energy to the interface for evaporation. $\dot{m}(h_v\text{-}h_l)$ stands for enthalpy of phase change and $\frac{1}{2}\dot{m}^3(\frac{1}{\rho_l{}^2} - \frac{1}{\rho_v{}^2})$ stands for change of kinetic energy of molecules leaving liquid phase and enter to the vapor phase. In the range of studied evaporation rate, the kinetic term at the interface $\frac{1}{2}\dot{m}^3(\frac{1}{\rho_l{}^2} - \frac{1}{\rho_v{}^2})$, is a few orders of magnitude smaller than the enthalpy term and is neglected. Having the temperature field along the interface and consequently heat fluxes, we used **Eq. 2** to determine local mass fluxes at different horizontal coordinates. **Table 2** shows the local mass fluxes at different horizontal coordinates for three set of experiments. Also, *average* mass flux measured by probing the temporal position of liquid-vapor is tabulated. As shown, the average mass flux is not in agreement with the measured local mass fluxes. This indicates that mass flux is not uniform across the interface. When there is a contact line (i.e. periphery of the container), due to small thermal conduction path from the solid to the liquid-vapor interface, the evaporation mass flux is much higher than that of the centerline. This non-uniform mass flux is shown in a range of previous studies[21,19,16,18]. The last radial coordinate that we probed the thermal field was 4 mm away from the periphery (i.e. the inner radius of the container was 22 mm and the last measured radial coordinate was 18 mm). The limitation in the radial motion of the automated thermocouple did not allow us to approach closer to the contact line. Note that the contact line area with diverging mass flux is in order of micrometer[22–24] and with the current instrumentation, we could not detect the temperature field at the contact line. Furthermore, as we increased evaporative mass flux by reducing the vapor pressure, we observed more uniform mass flux across the liquid-vapor interface and the role of non-uniform evaporation becomes less important. Due to symmetry condition at the centerline, thermal conduction is the only mode of energy transport and the local mass flux at the centerline could be used to examine evaporation theories.

A summary of all the experimental results is presented in **Table 1**. There exists a temperature discontinuity (i.e. temperature jump) of ~0.4 °C across the liquid–vapor interface in all the experiments which is much smaller than the value reported in previous studies[25,10,13] at the same pressure.

**Table 1**. Summary of evaporation experiment at different thermodynamic conditions

| $P_v$ (Pa) | $P_s$ (Pa) | Averaged $\dot{m} \times (10^4)$ ($kgm^{-2}s^{-1}$) | $\dot{m} \times (10^4)$ ($kgm^{-2}s^{-1}$) At centerline | $T_l$ (°C) | $T_v$ (°C) | $T_v$-$T_l$ (°C) | $\dot{q}_l$ ($Wm^{-2}$) | $\dot{q}_v$ ($Wm^{-2}$) | $L_{ww} \times (10^8)$ ($kgm^{-4}s$) ($k_h$=0.18) | $L_{qq} \times (10^{-4})$ ($kgs^{-3}$) ($k_h$=0.18) | $L_{qw}$ ($kgm^{-2}s^{-1}$) ($k_h$=0.18) |
|---|---|---|---|---|---|---|---|---|---|---|---|
| *No heating* | | | | | | | | | | | |
| 882 | 883.8 | 2.45 | 0.39 | 5.2 | 5.6 | 0.4 | 86 | -10.36 | 4.23 | 0.37 | -0.019 |
| 755 | 756.8 | 2.54 | 0.72 | 3 | 3.4 | 0.4 | 169 | -10.56 | 7.37 | 0.028 | -0.033 |
| 650 | 650.9 | 2.75 | 1.23 | 0.9 | 1.4 | 0.5 | 297 | -11.8 | 11.99 | 0.13 | -0.054 |
| 541 | 541.36 | 2.87 | 1.87 | -1.6 | -1.1 | 0.5 | 456 | -13.34 | 18.81 | 0.31 | -0.085 |
| 436 | 436.18 | 3.1 | 2.53 | -4.5 | -4 | 0.5 | 619 | -14.65 | 25.96 | 0.42 | -0.117 |
| 360 | 360.25 | 3.17 | 2.45 | -7 | -6.3 | 0.7 | 600 | -15.84 | 17.91 | 0.31 | -0.08 |
| *Heater at 40 °C* | | | | | | | | | | | |
| 913 | 913.15 | 3.78 | 1.77 | 5.7 | 6.1 | 0.4 | 433.2 | -10.59 | 24.77 | 0.236 | -0.111 |
| 734 | 734.06 | 4.12 | 1.89 | 2.6 | 3 | 0.4 | 462 | -10.65 | 25.84 | 0.583 | -0.117 |
| 636 | 636.4 | 3.99 | 2.18 | 0.6 | 1 | 0.4 | 534 | -12.15 | 27.54 | 0.138 | -0.124 |
| 541 | 541.4 | 4.5 | 2.24 | -1.6 | -1.1 | 0.5 | 549 | -12.93 | 22.52 | 0.22 | -0.101 |
| 446 | 446.15 | 4.62 | 3.1 | -4.2 | -3.8 | 0.4 | 762 | -16 | 39.04 | 0.52 | -0.176 |
| 374 | 374.22 | 4.62 | 3.61 | -6.5 | -6 | 0.5 | 894 | -13.5 | 35.26 | 0.095 | -0.159 |
| *Heater at 55 °C* | | | | | | | | | | | |
| 907 | 907.15 | 5.1 | 2.79 | 5.6 | 6 | 0.4 | 690 | -9.55 | 39.43 | 0.38 | -0.178 |
| 739 | 741.4 | 5.3 | 2.61 | 2.7 | 3.1 | 0.4 | 642 | -11.2 | 39.88 | 0.763 | -0.179 |
| 613 | 613.2 | 5.6 | 2.63 | 0.1 | 0.5 | 0.4 | 648 | -12 | 34.04 | 0.354 | -0.153 |
| 514 | 514.1 | 5.7 | 2.73 | -2.3 | -1.9 | 0.4 | 672 | -12.96 | 35.36 | 0.542 | -0.159 |
| 377 | 379 | 5.9 | 4.02 | -6.4 | -6 | 0.4 | 996 | -12.8 | 60.09 | 0.965 | -0.271 |
| *Heater at 70 °C* | | | | | | | | | | | |
| 604 | 604.14 | 6.8 | 2.92 | -0.1 | 0.3 | 0.4 | 720 | -12.64 | 37.95 | 0.473 | -0.171 |
| 526 | 526.11 | 6.96 | 3.4 | -2 | -1.6 | 0.4 | 840 | -12.16 | 45.2 | 0.435 | -0.204 |
| 360 | 360.1 | 7.1 | 4.43 | -7 | -6.6 | 0.4 | 1098 | -14.88 | 54.15 | 0.419 | -0.244 |

**Table 2**. Local mass fluxes at different radial coordinates along the liquid-vapor interface

| | Averaged mass flux | Position (a) (X = 0 cm) (Centerline) | Position (b) (X = 0.2 cm) | Position (c) (X = 0.6 cm) | Position (d) (X = 1 cm) | Position (e) (X = 1.4 cm) | Position (f) (X = 1.8 cm) |
|---|---|---|---|---|---|---|---|
| $\dot{m} \times (10^4)$ ($kgm^{-2}s^{-1}$) ($P_V$ = 428 Pa) | 2.91 | 2.46 | 2.58 | 2.53 | 2.51 | 2.49 | 2.28 |
| $\dot{m} \times (10^4)$ ($kgm^{-2}s^{-1}$) ($P_V$ = 566 Pa) | 2.82 | 1.94 | 1.72 | 2.12 | 2.67 | 2.98 | 3.05 |
| $\dot{m} \times (10^4)$ ($kgm^{-2}s^{-1}$) ($P_V$ = 763 Pa) | 2.63 | 0.42 | 0.61 | 0.86 | 1.34 | 1.70 | 1.96 |

## Theoretical analysis

By integrating the entropy equation over a control volume which consists of both liquid and vapor phases, the following equation is derived for entropy production at the interface.[26]

$$\dot{S}_{ir} = \dot{q}_v \left(\frac{1}{T_v} - \frac{1}{T_l}\right) - \dot{m}\left(\frac{1}{T_l}\right)(\mu_v - \mu_l) \tag{3}$$

Where $\mu_v$ and $\mu_l$ denotes the chemical potentials at vapor and liquid sides, respectively, $\dot{S}_{ir}$ is the entropy production and $T_v$ and $T_l$ are temperatures at vapor and liquid sides, respectively. Based on NET, this irreversible entropy production is defined as a sum of all thermodynamic forces multiplied with their respective fluxes[8].

$$\dot{S}_{ir} = \sum_i J_i X_i \tag{4}$$

Where $J_i$ represents fluxes and $X_i$ represents thermodynamic forces. The fluxes are linearly related to the all thermodynamic forces responsible for the fluxes.

$$J_i = \sum_i L_{ij} X_j \tag{5}$$

Considering the vapor phase as an ideal gas, **Eq. 3** is derived from **Eq. 7** during evaporation process for the net mass flux and the heat flux on the vapor side. The matrix of Onsager transfer coefficients is symmetric implying $L_{qw} = L_{wq}$ and there exist only three independent transfer coefficients describing the transport of heat and mass across the interface. Another equation is needed to close the system of equations. Coupling coefficient ($K_h$) is introduced and defined as[26,27]

$$K_h = \frac{-L_{qw}}{h_{lv} \times L_{ww}} = \left(\frac{-\dot{q}_v}{h_{lv} \times \dot{m}}\right)_{\Delta T=0} = \left(\frac{r_{q,w}^{v,l}}{h_{lv} \times r_{q,q}^{v,l}}\right)_{\Delta T=0} \tag{6}$$

Where $r_{q,w}^{v,l}$ and $r_{q,q}^{v,l}$ are resistivity transfer coefficients. Based on kinetic theory of gasses, Bedeaux et al[28] derived the following equations for resistivity transfer coefficients.

$$\begin{aligned} r_{q,w}^{v,l} &= \frac{\sqrt{\pi}}{8C_{eq}^{v}(T_v) \times T_v \times V_{mp}(T_v)} \times \left(1 + \frac{16}{5\pi}\right) \\ r_{q,q}^{v,l} &= \frac{\sqrt{\pi}}{4C_{eq}^{v}(T_v) \times R \times T_v^2 \times V_{mp}(T_v)} \times \left(1 + \frac{104}{25\pi}\right) \end{aligned} \tag{7}$$

Where $V_{mp}(T_v) = \sqrt{\frac{2RT_v}{M}}$ is the most probable thermal velocity, M is the molar mass, R is the gas constant and $C_{eq}^{v}(T_v)$ is molar density. According to the kinetic theory, $h_{lv}$ is equal to 2.5 $RT_v$. Substituting the value of $h_{lv}$ and values of $r_{q,w}^{v,l}$ and $r_{q,q}^{v,l}$ from Eq. 9 in Eq. 8, the value of 0.18 is obtained for $K_h$. In this study, by using Eq. 3 and considering the coupling coefficient ($K_h$) as 0.18, all transfer coefficients were calculated in each experiment and are presented in **Table 1**. Our analysis indicates that values of $L_{ww}$ and $L_{qw}$ are a function of mass flux at the interface and are not constant values. We plotted the determined coefficients as function of mass flux in **Fig. 20**.

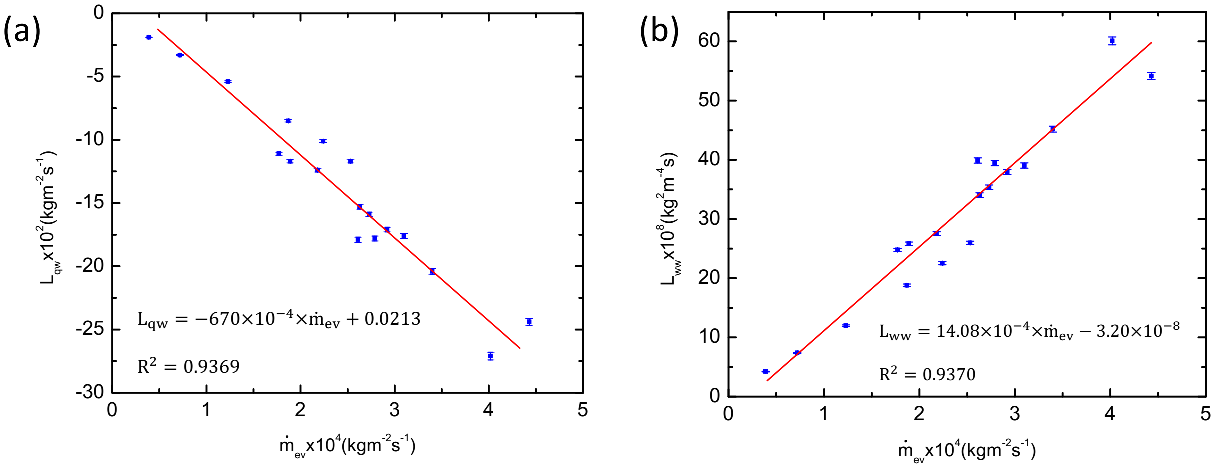

**Figure 20.** The transfer coefficient of (a) $L_{qw}$ and (b) $L_{ww}$ as function of net mass flux during evaporation is shown. Note that these experiments are conducted at a wide range of liquid temperatures and vapor pressures.

As show in **Fig. 5**, transfer coefficients $L_{ww}$ and $L_{qw}$ are found to be approximate linear functions of mass flux with the following expressions.

$$\begin{gathered} L_{ww} = 14.08\times10^{-4}\times\dot{m}_{ev} - 3.20\times10^{-8} \\ L_{qw} = -670\times\dot{m}_{ev} + 0.0213 \end{gathered} \tag{8}$$

Thus, by substitution of these expressions of coefficients in the **Eq. 3**, one obtains a predictive model of evaporation only based on interfacial thermodynamic properties written as

$$\dot{m}_{ev} = \frac{0.00001477 T_v T_l \ln[\frac{P_v}{P_s\,(T_l)}] - 0.0213(T_v - T_l)}{T_v - 670(T_v - T_l) + 0.6498 T_v T_l \ln[\frac{P_v}{P_s\,(T_l)}]} \tag{9}$$

Note that the Onsager terms may depend on nature of molecules interaction of the liquids. We may not extend this formula to all fluids before further studies.

## Examination of the predictive model for the evaporation mass flux

Since the mass flux in this predictive model is obtained in terms of experimentally measurable parameters, it can be examined with other studies. In the steady-state evaporation study by Kazemi et al.[12], temperature profile was measured at the centerline near the interface of water as it evaporated under low pressures. The mass flux at each pressure was measured and the reported values obtained are listed in **Table 3**.

**Table 3**. Summary of evaporation experiment reported in Kazemi et al.[12]

| Measured $\dot{m} \times 10^4$ ($kgm^{-2}s^{-1}$) | $P_v$ (Pa) | $P_s$ (Pa) | $T_l$ (°C) | $T_v$ (°C) | Predicted $\dot{m} \times 10^4$ ($kgm^{-2}s^{-1}$) |
|---|---|---|---|---|---|
| 3.60 | 265.7 ± 1.3 | 265.97 | -10.82 ± 0.05 | -10.46 ± 0.05 | 3.63 |
| 3.37 | 303.2 ± 1.5 | 303.66 | -9.15 ± 0.05 | -8.82 ± 0.05 | 3.37 |
| 3.21 | 369.4 ± 1.8 | 370.19 | -6.69 ± 0.05 | -6.40 ± 0.05 | 3.26 |
| 3.17 | 435.7 ± 2.2 | 436.94 | -4.52 ± 0.05 | - 4.28 ± 0.05 | 3.21 |
| 2.53 | 544.6 ± 2.7 | 545.79 | -1.61 ± 0.05 | -1.40 ± 0.05 | 2.59 |
| 2.11 | 672.5 ± 3.4 | 675.23 | 1.39 ± 0.05 | 1.56 ± 0.05 | 2.16 |
| 1.92 | 815.5 ± 4.1 | 819.19 | 4.08 ± 0.05 | 4.22 ± 0.05 | 1.94 |

**Equations 1 and 8** are used to predict the net mass flux based on the measured thermodynamic properties in the **Table 3**. The predicted mass flux by the developed model here and measured mass fluxes are compared in **Fig. 21**.

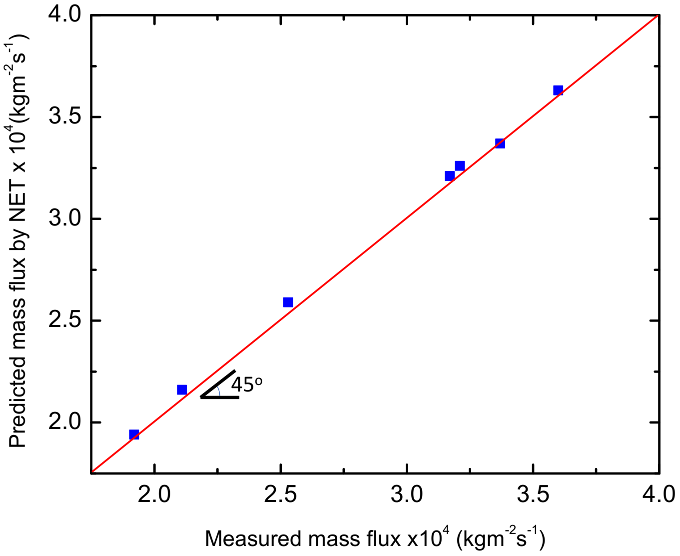

**Figure 21.** The predicted mass flux by the developed model is compared with the reported mass flux by Kazemi et al.[12] The excellent agreement by an independent set of experiments is another validation of the developed model.

According to **Fig. 6**, there is an excellent agreement between the predictions and the measurements. This agreement supports the developed predictive model and suggest a tool that could be used in all liquid-vapor phase change studies.

**Task 2: Mont-Carlo simulation of vapor Knudsen layer**

Here, we studied molecular-scale phenomena at liquid-vapor interface through solution of Boltzmann Transport Equation (BTE). This equation at the interface is written as

$$\frac{\partial f}{\partial x}(r, v_1, t) + \overrightarrow{v_1}\,.\,\nabla_{\vec{r}} f(r, v_1, t) + \frac{\vec{F}}{m}.\nabla_{\overrightarrow{v_1}} f(r, v_1, t) = \int d^3 v_2 \int d\sigma(\Omega)\,[f_1' f_2' - f_1 f_2]|\overrightarrow{v_1} - \overrightarrow{v_2}|$$

We solved the BTE equation through Mont-Carlo simulation of vapor phase adjacent to an evaporating liquid-vapor interface. We used SPARTA package to simulate vapor molecules. The working fluid was water and we develop the reference sub-code for water. As shown in **Fig. 22**, the 2D simulation domain has width of 100 $\mu m$ and the height of $n\lambda$, where $\lambda$ denote mean free path of vapor molecules. The boundary conditions at y = 0 is influx of vapor molecules and the boundary condition at y = $n\lambda$, is constant temperature. The boundary condition in x = 0 and x = 100 $\mu m$ are specular boundary condition. The boundary condition at y = $n\lambda$ varies from different reported data.

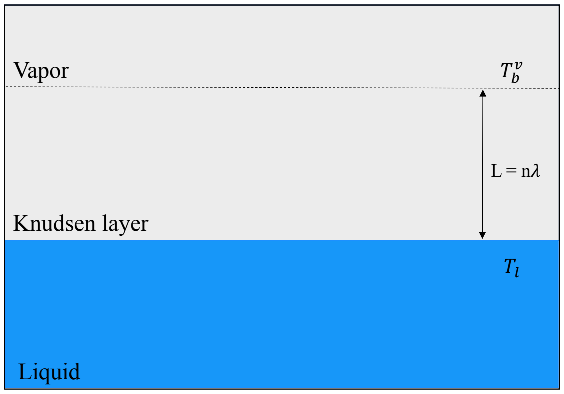

**Figure 22.** The domain to solve BTE to determine interfacial boundary condition during evaporation.

The measured temperature discontinuity by various groups as a function of mass flow rate are shown in **Fig. 23**. The results suggest that the measured temperature discontinuity for a given mass flow rate varies by two orders of magnitude which cannot be physically meaningful.

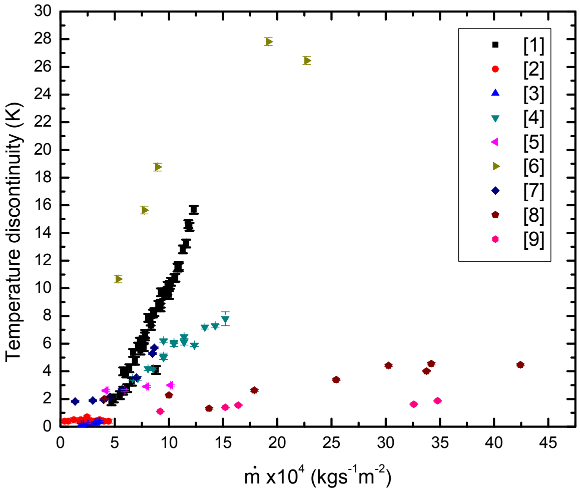

**Figure 23.** Measured temperature discontinuity as a function of mass flux at liquid-vapor interface.

Thus, through simulation of characteristics of vapor phase in the Knudsen layer, we determined temperature profile in the Knudsen layer for a given boundary condition. An example of temperature profile is shown in **Fig. 24**.

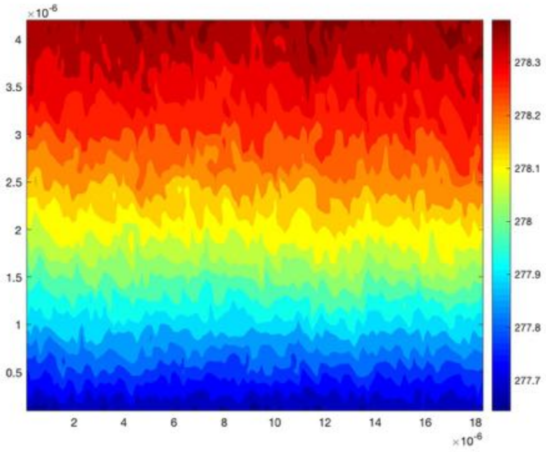

**Figure 24.** Simulation of temperature field of vapor molecules in the Knudsen layer.

Figure 9 suggests that temperature of vapor molecules that leave liquid-vapor interface equilibrate with the imposed temperature field by the boundary condition. That is, the measured vapor temperature at top of Knudsen layer does not reflect interracial vapor temperature of an evaporating liquid-vapor interface. This suggest that the high values of measured temperature discontinuity are artifact of the experimental setup and could not be used in any evaporation theory. To determine the correct temperature discontinuity at an evaporating interface, the supplied heat flux by the vapor phase should be close to zero. This study is ongoing to determine the correct temperature discontinuity at an evaporating liquid-vapor interface.

## Task 3: Ultra high heat flux in nano-confined geometries

Miniaturization has been the hallmark of electronic and photonic instruments in the last few decades. The miniaturization efforts span in an enormous range of dimension from nanoscale transistors to thumbnail-sized chips, smartphone, vehicle electronic and server farms. This miniaturization accompanied by enhanced functional density necessitates enhanced heat dissipation, which has been the bottleneck of further advancement in these technologies[29]. The current CPU power densities have reached to several hundred Watt per square centimeter. This constantly growing CPU power density has introduced a high demand for advanced cooling systems[30]. A range of approaches has been studied to address this high heat dissipation challenge including jet impingement[31], sprays[32] and micro-channels[33,34]. However, thin film evaporation with nanometer fluid thickness is considered as one of the most promising approaches to address the future technological demands[22,35,44–46,36–43]. The thickness of liquid film in this phenomenon should be in nanometer scale to reduce thermal resistance for heat transfer. Thin film evaporation phenomenon in micro/nanostructures is a coupled multi-physics momentum transport, energy transport, and gas kinetics problem. The momentum transport governs the liquid flow to the liquid-vapor interface; the energy transport governs the heat transfer to the interface, and the gas kinetics governs the evolution of molecules from liquid phase to the vapor phase. Depending on time scale, length scale, and the thermodynamic properties of the liquid-vapor interface, each of these physics imposes a limit on the kinetics of thin film evaporation. Currently, momentum transport is the limiting factor nor diffusion and kinetics of liquid molecules transformation to vapor phase. Although great strides have been made to achieve higher limits, much work remains to be done to reach gas kinetics limit of evaporation.

Here, we utilized concept of liquid absolute negative pressure and *slip boundary condition* in nanochannels to achieve unprecedented heat fluxes through thin-film evaporation. To achieve negative pressure at the liquid-vapor interface, we fabricated an array of closed nanochannels as shown in **Fig. 25a**. The fabrication processes were discussed in the previous report. The developed structure is made up of 9 sets of nanochannels and two micro-reservoirs placed perpendicularly along the two ends of the nanochannels. Each set of nanochannels consists of 11 separate channels with width of 6 μm, depth of (40-100 nm) and length of 1.6 mm. The reservoirs are 2 mm in width, 4 mm in length and 25 μm in depth. These micro-reservoirs pump the liquid to the channels via capillary force for evaporation. The geometry of the channels was examined with Scanning Probe Microscopy (SPM). As shown, the developed channels are highly uniform and consistent. This consistency allows us to have a sound interpretation of the experimental results. To achieve slip boundary condition at solid-liquid interface, we grafted monolayer of graphene on the developed Si nanochannels through direct transfer method. The profile of the nanochannels after Graphene transfer is shown in **Fig. 25**.

As shown, the Graphene monolayer has not affected profile of nanochannels. Once developed, the Graphene structure is probed with Raman Spectroscopy as shown in **Fig. 26**. The spectrum shows structure of Graphene with some defects. To finalize development of channels, the channels are sealed with borosilicate glass with a thickness of 1.1 mm through anodic bonding. The developed nanochannels were cleaned thoroughly before the experiments through plasma cleaning. We chose isopropyl alcohol as the working liquid in all experiments as it provides complete wettability of Si nanochannels and contact angle close to zero.

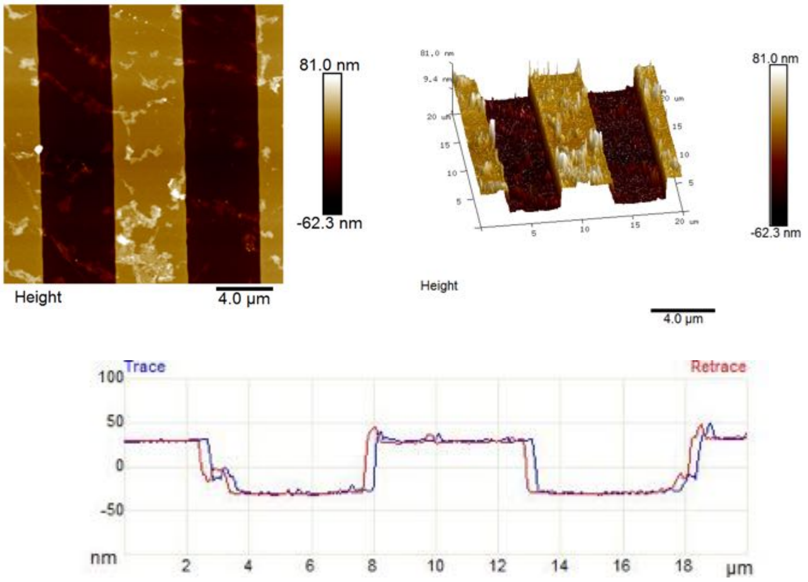

**Figure 25**. The profile of Si nanochannels with grafted monolayer of Graphene. Direct transfer method enabled us to have a uniform profile in the channels.

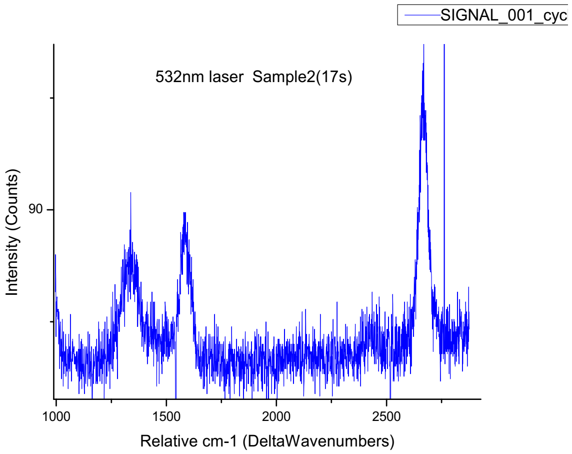

**Figure 26**. Raman spectroscopy of nanochannels after being transferred on the Si nanochannels. The peaks shows that the transferred Graphene has low defects.

Initially, we looked at wetting characteristics of these nanochannels. This provide a good insight on the solid-liquid boundary condition. The wetting dynamics of working fluid in these channels is shown in **Fig. 27a**. This dynamic is plotted for four representative channels. The results demonstrate that velocity and consequently mass flow rate in these channels compared to Si nanochannels is an order of magnitude higher. That is, slip boundary condition in these channels has provided a unique tool to overcome momentum transport limit in these nanochannels. We also studied de-wetting characteristics of these nanochannels in **Fig. 27b**. De-wetting velocity in these channels is also an order of magnitude faster than Si nano-channels. Theoretical analysis is ongoing to provide a predictive model for wetting and de-wetting of these channels. The finding of the study shows that through nano-scale confinement of fluid and slip boundary condition at solid-liquid interface, one could develop spreaders for extreme heat dissipation.

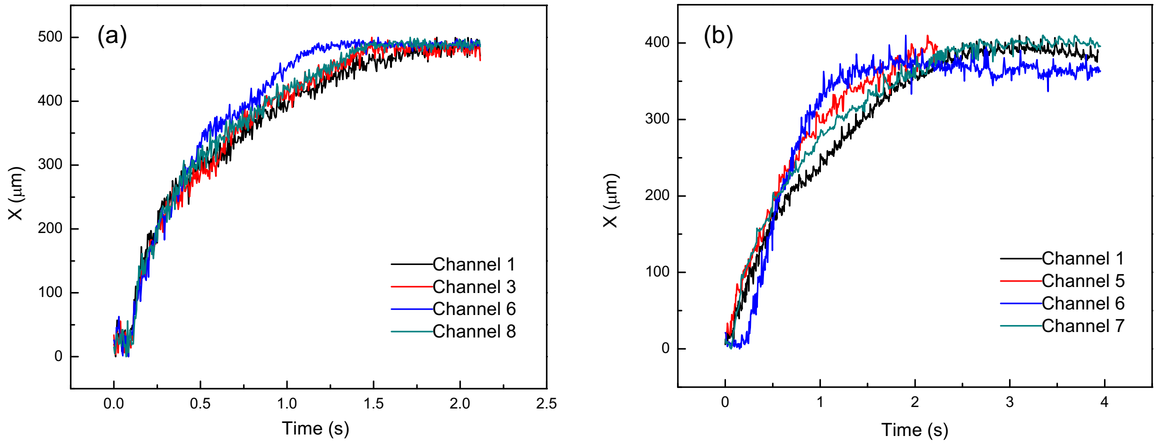

**Figure 27.** Wetting and De-Wetting characteristics of Graphene grafted nanochannels. The velocity in these channels is an order of magnitude higher than Si nanochannels.

## References

(1) Hertz, H. Ueber Die Verdunstung Der Flüssigkeiten, Insbesondere Des Quecksilbers, Im Luftleeren Raume. *Ann. Phys.* **1882**, *17*, 177–193.

(2) Knudsen, M. Die Maximale Verdampfungsgeschwindigkeit Des Quecksilbers. *Ann. Phys.* **1915**, *47*, 697–708.

(3) Schrage, R. W. *A Theoretical Study of Interphase Mass Transfer*; Columbia university press: New York, 1953.

(4) Ward, C. A.; Findlay, R. D.; Rizk, M. Statistical Rate Theory of Interfacial Transport. I. Theoretical Development. *J. Chem. Phys.* **1982**, *76*, 5599–5605.

(5) Ward, C. A.; Findlay, R. D. Statistical Rate Theory of Interfacial Transport. IV. Predicted Rate of Dissociative Adsorption. *J. Chem. Phys.* **1982**, *76*, 5615–5623.

(6) Ward, C. A.; Elmoselhi, M. Molecular Adsorption at a Well Defined Gas-Solid Interphase: Statistical Rate Theory Approach. *Surf. Sci.* **1986**, *176*, 457–475.

(7) Kapoor, A.; Elliott, J. A. W. Nonideal Statistical Rate Theory Formulation To Predict Evaporation Rates from Equations of State. *J. Phys. Chem. B* **2008**, *112*, 15005–15013.

(8) Callen, H. B. *Thermodynamics and an Introduction to Thermostatistics*; Second edi.; John Wiley & Sons, Inc., 1985.

(9) Jou, D.; Casas-Vazquez, J.; Lebon, G. *Extended Irreversible Thermodynamics*; Springer, 1996.

(10) Badam, V. K.; Kumar, V.; Durst, F.; Danov, K. Experimental and Theoretical Investigations on Interfacial Temperature Jumps during Evaporation. *Experim. Therm. Fluid Sci.* **2007**, *32*, 276–292.

(11) Bedeaux, D.; Kjelstrup, S.; Bedeauxa, D. Transfer Coefficients for Evaporation. *Physica A* **1999**, *270*, 413–426.

(12) Kazemi, M. A.; Nobes, D. S.; Elliott, J. A. W. Experimental and Numerical Study of the Evaporation of Water at Low Pressures. *Langmuir* **2017**, *33*, 4578–4591.

(13) Fang, G.; Ward, C. A. Temperature Measured Close to the Interface of an Evaporating Liquid. *Phys. Rev. E* **1999**, *59*, 417–428.
(14) Ward, C. A.; Duan, F. Turbulent Transition of Thermocapillary Flow Induced by Water Evaporation. *Phys. Rev. E* **2004**, *69*, 56308.
(15) Ward, C. A.; Fang, G. Expression for Predicting Liquid Evaporation Flux: Statistical Rate Theory Approach. *Phys. Rev. E - Stat. Physics, Plasmas, Fluids, Relat. Interdiscip. Top.* **1999**, *59*, 429–440.
(16) Hu, H.; Larson, R. G. Evaporation of a Sessile Droplet on a Substrate. *J. Phys. Chem. B* **2002**, *106*, 1334–1344.
(17) Ghasemi, H.; Ward, C. A. Energy Transport by Thermocapillary Convection during Sessile-Water-Droplet Evaporation. *Phys. Rev. Lett.* **2010**, *105*.
(18) Ristenpart, W. D.; Kim, P. G.; Domingues, C.; J.Wan; Stone, H. A. Influence of Substrate Conductivity on Circulation Reversal in Evaporating Drops. *Phys. Rev. Lett.* **2007**, *99*.
(19) Dehaeck, S.; Rednikov, A.; Colinet, P. Vapor-Based Interferometric Measurement of Local Evaporation Rate and Interfacial Temperature of Evaporating Droplets. *Langmuir* **2014**, *30*, 2002–2008.
(20) Mills, A. F. *Basic Heat Mass Transfer*; Marica Horton, Ed.; Second.; Prentice Hall: New Jersey, 1999.
(21) Ghasemi, H.; Ward, C. A. Energy Transport by Thermocapillary Convection during Sessile-Water-Droplet Evaporation. *Phys. Rev. Lett.* **2010**, *105*, 136102.
(22) Wang, H.; Garimella, S. V.; Murthy, J. Y. An Analytical Solution for the Total Heat Transfer in the Thin-Film Region of an Evaporating Meniscus. *Int. J. Heat Mass Transf.* **2008**, *51*, 6317–6322.
(23) Wang, H.; Garimella, S. V.; Murthy, J. Y. Characteristics of an Evaporating Thin Film in a Microchannel. *Int. J. Heat Mass Transf.* **2007**, *50*, 3933–3942.
(24) Farokhnia, N.; Irajizad, P.; Sajadi, S. M.; Ghasemi, H. Rational Micro/Nanostructuring for Thin-Film Evaporation. *J. Phys. Chem. C* **2016**, *120*, 8742–8750.
(25) Duan, F.; Badam, V. K.; Durst, F.; Ward, C. A. Thermocapillary Transport of Energy during Water Evaporation. *Phys. Rev. E* **2005**, *72*, 56303.
(26) Bedeaux, D.; Kjelstrup, S. Transfer Coefficients for Evaporation. *Phys. A Stat. Mech. its Appl.* **1999**, *270*, 413–426.
(27) Kjelstrup, S.; Bedeaux, D. *Non-Equilibrium Thermodynamics of Heterogeneous Systems*; World Scientific: Singapore, 2008.
(28) Bedeaux, D.; Ytrehus, T. Slow Evaporation. **1992**, *182*, 388–418.
(29) Cho, J.; Goodson, K. E. Thermal Transport: Cool Electronics. *Nat. Mater.* **2015**, *14*, 136–137.
(30) Pop, E. Energy Dissipation and Transport in Nanoscale Devices. *Nano Res.* **2010**, *3*, 147–169.
(31) Browne, E. a.; Jensen, M. K.; Peles, Y. Microjet Array Flow Boiling with R134a and the Effect of Dissolved Nitrogen. *Int. J. Heat Mass Transf.* **2012**, *55*, 825–833.
(32) Horacek, B.; Kiger, K. T.; Kim, J. Single Nozzle Spray Cooling Heat Transfer Mechanisms. *Int. J. Heat Mass Transf.* **2005**, *48*, 1425–1438.
(33) Zhang, T.; Peles, Y.; Wen, J. T.; Tong, T.; Chang, J. Y.; Prasher, R.; Jensen, M. K. Analysis and Active Control of Pressure-Drop Flow Instabilities in Boiling Microchannel Systems. *Int. J. Heat Mass Transf.* **2010**, *53*, 2347–2360.
(34) Kandlikar, S. G.; Bapat, A. V. Evaluation of Jet Impingement, Spray and Microchannel

Chip Cooling Options for High Heat Flux Removal. *Heat Trans. Eng.* **2007**, *28*, 911–923.

(35) Wayner, P. C.; Kao, Y. K.; LaCroix, L. V. The Interline Heat-Transfer Coefficient of an Evaporating Wetting Film. *Int. J. Heat Mass Transf.* **1976**, *19*, 487–492.

(36) Ranjan, R.; Murthy, J. Y.; Garimella, S. V. Analysis of the Wicking and Thin-Film Evaporation Characteristics of Microstructures. *J. Heat Transfer* **2009**, *131*, 101001.

(37) Jiao, a. J.; Ma, H. B.; Critser, J. K. Evaporation Heat Transfer Characteristics of a Grooved Heat Pipe with Micro-Trapezoidal Grooves. *Int. J. Heat Mass Transf.* **2007**, *50*, 2905–2911.

(38) Narayanan, S.; Fedorov, A. G.; Joshi, Y. K. On-Chip Thermal Management of Hotspots Using a Perspiration Nanopatch. *J. Micromech. Microeng.* **2010**, *20*, 075010.

(39) Plawsky, J. L.; Fedorov, a G.; Garimella, S. V; Ma, H. B. Nano- and Microstructures for Thin-Film Evaporation — A Review. *Nanosc. Microsc. Thermophys. Eng.* **2014**, *18*, 251–269.

(40) Yan, C.; Ma, H. B. Analytical Solutions of Heat Transfer and Film Thickness in Thin-Film Evaporation. *J. Heat Transf.* **2013**, *135*, 031501.

(41) Su, F.; Ma, H.; Han, X.; Chen, H.-H.; Tian, B. Ultra-High Cooling Rate Utilizing Thin Film Evaporation. *Appl. Phys. Lett.* **2012**, *101*, 113702.

(42) Ma, H. B.; Cheng, P.; Borgmeyer, B.; Wang, Y. X. Fluid Flow and Heat Transfer in the Evaporating Thin Film Region. *Microfluid. Nanofluid.* **2008**, *4*, 237–243.

(43) Narayanan, S.; Fedorov, A. G.; Joshi, Y. K. Interfacial Transport of Evaporating Water Confined in Nanopores. *Langmuir* **2011**, *27*, 10666–10676.

(44) Bar-Cohen, a.; Sherwood, G.; Hodes, M. Gas-Assisted Evaporative Cooling of High Density Electronic Modules. In *Proceedings of 4th Intersociety Conference on Thermal Phenomena in Electronic Systems (I-THERM)*; Washington, DC, 1994; Vol. 18, pp. 32–40.

(45) Dhavaleswarapu, H. K.; Garimella1, S. V; Murthy, J. Y.; Garimella, S. V. Microscale Temperature Measurements Near the Triple Line of an Evaporating Thin Liquid Film. *J. Heat Transf.* **2009**, *131*, 061501.

(46) Migliaccio, C. P.; Dhavaleswarapu, H. K.; Garimella, S. V. Temperature Measurements near the Contact Line of an Evaporating Meniscus V-Groove. *Int. J. Heat Mass Transf.* **2011**, *54*, 1520–1526.

# AFOSR Deliverables Submission Survey

Response ID:12019 Data

## 1.

**Report Type**

Final Report

**Primary Contact Email**
**Contact email if there is a problem with the report.**

hghasemi@uh.edu

**Primary Contact Phone Number**
**Contact phone number if there is a problem with the report**

713-743-6183

**Organization / Institution name**

University of Houston

**Grant/Contract Title**
**The full title of the funded effort.**

Toward Bio-Inspired Smart Thermal Spreaders (BSTS)

**Grant/Contract Number**
**AFOSR assigned control number. It must begin with "FA9550" or "F49620" or "FA2386".**

FA9550-16-1-0248

**Principal Investigator Name**
**The full name of the principal investigator on the grant or contract.**

Hadi Ghasemi

**Program Officer**
**The AFOSR Program Officer currently assigned to the award**

Dr. Ali Sayir

**Reporting Period Start Date**

05/01/2016

**Reporting Period End Date**

07/30/2019

**Abstract**

In this research program, we aimed to understand fundamentals of liquid- vapor phase change at small-scale and to develop a bio-inspired thermal spreader. In the first budget period, we developed a new concept and corresponding material structure that breaks the limit of phase-change heat transfer (Leidenfrost limit). The developed concept, decoupled hierarchical structures, is implemented in both Si and Cu structures. In the second budget period, we studied fundamentals of liquid-vapor phase change in a controlled evaporation chamber to tune and measure interfacial mass and heat transfer at an evaporating interface. We formed a predictive model based on the non-equilibrium thermodynamics that can predict mass and energy flux independently. In contrast with the current gas kinetics models, the developed model satisfies both momentum and energy conservations. This model provides groundwork for all the liquid- vapor phase-change studies. In the other task of this

research program, we studied limits of evaporative heat flux in nano-confined geometries. We studied thin-film evaporation in nanochannels under absolute negative pressure in both transient and steady-state conditions. The findings suggest that thin-film evaporation in nanochannels can be a bubble-free process even at temperatures higher than boiling temperature providing high reliability of thermal management systems. To achieve this bubble- free characteristic, the dimension of nanochannels should be smaller than critical nucleolus dimension. In steady-state condition, unprecedented heat flux of 14274 Wcm-2 is achieved in the nanochannels, which corresponds to liquid velocity of 0.26 ms-1. This ultra-high heat flux is demonstrated for a long-time period. The developed structure provides a rational route to design thermal management technologies for high-performance electronic/photonic devices.

In the third budget period, we studied interfacial phenomena at Knudsen layer adjacent to liquid-vapor interface. We solved Boltzmann Transport Equation (BTE) through Mont-Carlo simulation of vapor phase at the liquid-vapor interface. These simulations provided a molecular-scale insight on physical phenomena occurring at liquid-vapor interface. The determined temperature profile in Knudsen layer by these simulations addressed the long-debated temperature discontinuity at the liquid-vapor interface. Despite measured temperature discontinuity up to 15 oC at evaporating interface of liquid-vapor, we proved that the measured discontinuity is a function of vapor boundary condition and is not an intrinsic characteristic of liquid-vapor interface. This finding closes the discussion on the correct thermodynamic boundary conditions needed to be used to determine kinetics of evaporation. As we have a plan to achieve extreme heat fluxes close to kinetics limit, we tried to eliminate momentum limit of liquid transport through slip boundary condition at solid-liquid interface. Through a well-customized approach, we grafted monolayer of Graphene on nanochannels. The slip boundary condition imposed by Graphene resulted in an order of magnitude higher mass flux in the nanochannels. This higher mass flux provided a route to boost heat dissipation capacity of nanochannels and develop heat spreaders for extreme environments.

---

**Distribution Statement**

**This is block 12 on the SF298 form.**

Distribution A - Approved for Public Release

---

**Explanation for Distribution Statement**

**If this is not approved for public release, please provide a short explanation.  E.g., contains proprietary information.**

---

**SF298 Form**

**Please attach your SF298 form.  A blank SF298 can be found here.  Please do not password protect or secure the PDF  The maximum file size for an SF298 is 50MB.**

SF_298.pdf

---

**Upload the Report Document. File must be a PDF. Please do not password protect or secure the PDF . The maximum file size for the Report Document is 50MB.**

AFOSR_Final_Report-_FA9550-16-1-0248_P-1.pdf

---

**Upload a Report Document, if any. The maximum file size for the Report Document is 50MB.**

---

**Archival Publications (published) during reporting period:**

1) Varun Kashyap, Siwakorn Sakunkaewkasem, Parham Jafari, Masomeh Nazari, Bahareh Eslami, Sina Nazifi, Peyman Irajizad, Maria Marquez, T. Randall Lee and Hadi Ghasemi, "Full spectrum solar thermal energy harvesting and storage by a molecular and phase-change hybrid mate- rial", Joule, 2019.

2) Peyman Irajizad∗, Sina Nazifi∗ and Hadi Ghasemi. "Icephobic Surfaces: Definition and Figures of Merit ", Advances in Colloids and Interface Science, 2019.

3) Ali Masoudi∗, Parham Jafari∗, Varun Kashyap∗, Masoumeh Nazari∗ and Hadi Ghasemi. "In- situ studies on kinetics of hydrate formation", Review of Scientific Instruments, 90, 035111, 2019.

4) Peyman Irajizad, Abdullah Al-Bayati, Bahareh Eslamiz, Taha Shafquat, Masoumeh Nazari, Parham Jafari∗, Varun Kashyap∗, Ali Masoudi∗, Daniel Araya and Hadi Ghasemi, "Stress-Localized Durable Icephobic Surfaces", Materials

Horizons, 6, 758-766, 2019.

5) Masoumeh Nazari, Ali Masoudi∗, Parham Jafari, Varun Kashyap, Peyman Irajizad and Hadi Ghasemi. "Ultra heat flux in nano-confined geometries", Langmuir, 35, 1, 78-85, 2019.

6) Varun Kashyap∗, Riddhiman Medhi∗, Peyman Irajizad∗, Parham Jafari∗, Masoumeh Nazari∗, Ali Masoudi∗, Maria D. Marquez, T. Randall Lee, and Hadi Ghasemi, "Capture and conversion of carbon dioxide to water by solar heat localization", Sustainable Energy and Fuels, 3, 272- 279, 2019.

7) Parham Jafari∗, Ali Masoudi∗, Peyman Irajizad∗, Masoumeh Nazari∗, Varun Kashyap∗, Bahareh Eslami∗ and Hadi Ghasemi, "Evaporation mass flux: a predictive model and experiments, Langmuir, 34(39), 11676- 11684, 2018.

8) Seyed Mohammad Sajadi∗, Peyman Irajizad∗, Varun Kahshyap∗, Nazanin Farokhnia∗ and Hadi Ghasemi, 'Surfaces for high heat dissipation with no Leidenfrost limit". Applied Physics Letters, 111, 021605, 2017.

9) Seyed Mohammad Sajadi∗, Jose Ordonez-Miranda, James M. Hill, Younes Ezzahri, Karl Joulain and Hadi Ghasemi, "Invariant for One-Dimensional Heat Conduction in Dielectrics and Metals". Europhysics Letters, 118, 34001, 2017.

10) Ali Masoudi∗, Peyman Irajizad∗, Nazanin Farokhnia∗, Varun Kashyap∗ and Hadi Ghasemi, "Anti-scaling magnetic slippery surfaces", ACS Applied Materials and Interfaces, 9, 21025-21033, 2017.

11) Peyman Irajizad∗, Sahil Ray∗, Nazanin Farokhnia∗, and Hadi Ghasemi, "Remote droplet manip- ulation on self-healing thermally activated magnetic slippery surfaces"Advanced Materials Interfaces, 4, 1700009, 2017.

12) Nazanin Farokhnia∗, Seyed Mohammad Sajadi∗, Peyman Irajizad∗, and Hadi Ghasemi, "De- coupled hierarchical structures for suppression of Leidenfrost Phenomenon". Langmuir, 33 (10), 2541-2550, 2017.

13)Peyman Irajizad∗, Munib Hasnain∗, Nazanin Farokhnia∗, Seyed Mohammad Sajadi∗, and Hadi Ghasemi, "Magnetic slippery extreme icephobic surfaces". Nature Communications. 7, 13395, 2016.

**New discoveries, inventions, or patent disclosures:**

**Do you have any discoveries, inventions, or patent disclosures to report for this period?**

No

**Please describe and include any notable dates**

**Do you plan to pursue a claim for personal or organizational intellectual property?**

**Changes in research objectives (if any):**

NA

**Change in AFOSR Program Officer, if any:**

NA

**Extensions granted or milestones slipped, if any:**

3 months no cost extension

**AFOSR LRIR Number**

**LRIR Title**

**Reporting Period**

**Laboratory Task Manager**

**Program Officer**

**Research Objectives**

**Technical Summary**

**Funding Summary by Cost Category (by FY, $K)**

| | Starting FY | FY+1 | FY+2 |
|---|---|---|---|
| Salary | | | |
| Equipment/Facilities | | | |
| Supplies | | | |
| Total | | | |

**Report Document**

**Report Document - Text Analysis**

**Report Document - Text Analysis**

**Appendix Documents**

## 2. Thank You

**E-mail user**

Oct 29, 2019 15:04:59 Success: Email Sent to: hghasemi@uh.edu